EFDA–JET–PR(10)68

D. Van Eester, E. Lerche, T. Johnson, T. Hellsten, J. Ongena, M.-L. Mayoral, D. Frigione, C. Sozzi, G. Calabro, M. Lennholm, P. Beaumont, T. Blackman, D. Brennan, A. Brett, M. Cecconello, I. Coffey, A. Coyne, K. Crombé, A. Czarnecka, R. Felton, M. Gatu Johnson, C. Giroud, G. Gorini, C. Hellesen, P. Jacquet, Ye. Kazakov, V. Kiptily, S. Knipe, A. Krasilnikov, Y. Lin, M. Maslov, I. Monakhov, C. Noble, M. Nocente, L. Pangioni, I. Proverbio, M. Stamp, W. Studholme, M. Tardocchi, T.W. Versloot, V. Vdovin, A. Whitehurst, E. Wooldridge, V. Zoita and JET EFDA contributors

Heating (^{3}He)-H JET Plasmas with Multiple Mode Conversion Layers

Heating (^{3}He)-H JET Plasmas with Multiple Mode Conversion Layers

D. Van Eester[1], E. Lerche[1], T. Johnson[2], T. Hellsten[2], J. Ongena[1], M.-L. Mayoral[3], D. Frigione[4], C. Sozzi[5], G. Calabro[4], M. Lennholm[6], P. Beaumont[3], T. Blackman[3], D. Brennan[3], A. Brett[3], M. Cecconello[7], I. Coffey[3], A. Coyne[3], K. Crombe[8], A. Czarnecka[9], R. Felton[3], M. Gatu Johnson[7], C. Giroud[3], G. Gorini[5], C. Hellesen[7], P. Jacquet[3], Ye. Kazakov[10], V. Kiptily[3], S. Knipe[3], A. Krasilnikov[11], Y. Lin[12], M. Maslov[13], I. Monakhov[3], C. Noble[3], M. Nocente[5], L. Pangioni[3], I. Proverbio[5], M. Stamp[3], W. Studholme[3], M. Tardocchi[5], T.W. Versloot[14], V. Vdovin[15], A. Whitehurst[3], E. Wooldridge[3], V. Zoita[16] and JET EFDA contributors*

JET-EFDA, Culham Science Centre, OX14 3DB, Abingdon, UK

[1]LPP-ERM/KMS, Association EURATOM-'Belgian State', TEC Partner, Brussels, Belgium
[2]Fusion Plasma Physics, Association EURATOM-VR, KTH, Stockholm, Sweden
[3]EURATOM-CCFE Fusion Association, Culham Science Centre, OX14 3DB, Abingdon, OXON, UK
[4]Euratom-ENEA sulla Fusione, C. R. Frascati, Frascati, Italy
[5]Instituto di Fisica del Plasma, EURATOM-ENEA-CNR Association, Milan, Italy
[6]EFDA Close Support Unit, Culham Science Centre, Abingdon OX14 3DB, UK & European Commission, B-1049 Brussels, Belgium
[7]Uppsala University, Association EURATOM-VR
[8]Department of Applied Physics, Ghent University, B-9000 Ghent, Belgium
[9]Institute of Plasma Physics and Laser Microfusion, Warsaw, Poland, Uppsala, Sweden
[10]V.N. Karazin Kharkiv National University, Kharkiv, Ukraine
[11]SRC RF Troitsk Institute for Innovating and Fusion Research, Troitsk, Russia
[12]MIT Plasma Science and Fusion Center, Cambridge, MA 02139, USA
[13]CRPP-EPFL, Association EURATOM-Confédération Suisse, CH-1015 Lausanne, Switzerland
[14]FOM Institute Rijnhuizen, Association EURATOM-FOM, Nieuwegein, the Netherlands
[15]RNC Kurchatov Institute, Nuclear Fusion Institute, Moscow, Russia
[16]Association EURATOM-MEdC, National Institute for Plasma Physics, Bucharest, Romania
** See annex of F. Romanelli et al, "Overview of JET Results", (23rd IAEA Fusion Energy Conference, Daejon, Republic of Korea (2010)).*

Preprint of Paper to be submitted for publication in
Plasma Physics and Controlled Fusion

ABSTRACT

The constructive interference effect described by Fuchs et al. [1] shows that the mode conversion and thereby the overall heating efficiency can be enhanced significantly when an integer number of fast wave wavelengths can be folded in between the (high field side) fast wave cutoff and the ion-ion hybrid layer(s) at which the ion Bernstein or ion cyclotron waves are excited. This effect was already experimentally identified in (^{3}He)-D plasmas [2] and was recently tested in (^{3}He)-H JET plasmas [3]. The latter is a so-called 'inverted' scenario which differs significantly from the (^{3}He)-D scenarios since the mode-conversion layer is positioned between the low field side edge of the plasma and the ion-cyclotron layer of the minority ^{3}He ions (whereas the order in which an incoming wave encounters these layers is inverted in a 'regular' scenario), and because much lower ^{3}He concentrations are needed to achieve the mode conversion heating regime. Dominant electron heating with global heating efficiencies between 30% and 70% depending on the ^{3}He concentration were observed in the JET experiments. The unwanted presence of both ^{4}He and D in the discharges gave rise to 2 mode conversion layers rather than a single one. This together with the fact that the location of the high field side fast wave cutoff is a sensitive function of the parallel wave number and that one of the confluences' locations critically depends on the ^{3}He concentration makes the interpretation of the results more complex but also more interesting: Three regimes could be distinguished as a function of X[^{3}He]: (i) a regime at low concentration (X[^{3}He] <1.8%) at which ion cyclotron resonance frequency (ICRF) heating is efficient, (ii) a regime at intermediate concentrations (1.8<X[^{3}He]<5%) in which the RF performance is degrading and ultimately becoming very poor, and finally (iii) a good heating regime at ^{3}He concentrations beyond 6%. In this latter regime, the heating efficiency did not critically depend on the actual concentration while at lower concentrations (X[^{3}He]<4%) a bigger excursion in heating efficiency is observed and the estimates differ somewhat from shot to shot, and depending on whether local or global signals are chosen for the heating efficiency analysis. The different dynamics at the various concentrations can be traced back to the presence of 2 mode conversion layers and their associated fast wave cutoffs residing inside the plasma at low ^{3}He concentration. One of these layers is approaching and crossing the low field side plasma edge when 1.8<X[^{3}He]<5%. Adopting a minimization procedure to correlate the mode conversion positions with the plasma composition reveals that the different behaviors observed are due to contamination of the plasma by C, D and ^{4}He. Wave modeling not only supports this interpretation but also shows that moderate concentrations of such D-like species significantly alter the overall wave behavior in H-^{3}He plasmas. Whereas numerical modeling yields quantitative information on the heating efficiency, recent analytical work by Kazakov [4] permits to grasp the dominant underlying wave interaction physics.

1. INTRODUCTION

Mode conversion heating has become one of the standard tools to do transport analysis and is often used in rotation experiments (see e.g. [5, 6]). It relies on the mode conversion, at the Ion-Ion Hybrid

(IIH) resonance, of the Fast Wave (FW) launched by standard ICRF antennas, to shorter wavelength waves that are efficiently damped on electrons. The interference effect described by Fuchs et al. [1] allows to significantly enhance the mode conversion and thereby the overall RF heating efficiency when the machine and plasma parameters are chosen such that an integer number of FW wavelengths can be folded in between the High Field Side (HFS) FW cutoff and the IIH layer. This effect was already experimentally identified in (^{3}He)-D plasmas [2] and was recently tested in (^{3}He)-H JET plasmas. In the latter case, commonly referred to as an 'inverted scenario', the ion-ion hybrid layer is positioned between the antenna on the Low Field Side (LFS) and the ion cyclotron layer of the minority ^{3}He ions while in standard – e.g. (^{3}He)-D - scenarios the ion cyclotron layer is in between the IIH layer and the LFS.

Before going to its activated phase, ITER would be run at 2.65T i.e. half its nominal magnetic field and using Hydrogen plasmas. From the ICRF (ion cyclotron resonance frequency) heating point of view, H-(^{3}He) plasmas at 2.65T are an exact mock-up of the D-T plasmas: The Z/A values of H and ^{3}He ions (Z: charge number, A: mass number) differ by a factor of 2 with those of D and T and hence the relative positions of the cyclotron layers are identical when running at half the field. Recent JET experiments examined the potential of the fundamental (N = 1, where N is the cyclotron harmonic number) H majority heating (the topic of the present paper and briefly summarized in [3]) and the second harmonic (N = 2) ^{3}He heating at ITER's half field [7,8]. By merely changing the magnetic field to the more standard 3.4T, minority and mode conversion wave heating in (^{3}He)-H was also studied. Mayoral et al. examined the ICRF heating of such plasmas at very low ^{3}He concentrations (~1%) [9] and found that the mode conversion regime was already reached at X[^{3}He]~2-3%, in contrast to the ~10-15% needed to make the mode conversion efficient in regular scenarios. These experiments also brought to light the sensitivity of inverted scenarios to the plasmas composition: the Carbon unavoidably present in JET plasmas (up to 2010, the JET inner vessel was covered with C tiles) shifted the mode conversion layer over a distance of ~0.2m away from where it was expected to lie.

The more recent (^{3}He)-H experiments focused on studying the higher X[^{3}He] range and in particular addressed the questions "How can the mode conversion efficiency be optimized?" and "Can significant plasma flow be generated in the mode conversion regime?"

The paper is structured as follows: First, general information is given on the recent (^{3}He)-H experiments. Then the importance of the ^{3}He concentration, X[^{3}He], on the performance of the heating scenario is highlighted showing the dependence of some key experimental quantities on X[^{3}He]. The response of the plasma to RF power modulation is the subject of the next section. Subsequently the sensitivity of the mode conversion locations on the plasma composition is studied, and a section is devoted to wave induced fast particle populations. A short note on the obtained rotation data is equally included. After that, a section is devoted to the wave modeling. Finally, conclusions are drawn.

2. RECENT JET (^{3}HE)-H EXPERIMENTS

2.1. GENERAL REMARKS

During the recent mode conversion studies in JET in (^{3}He)-H plasmas two types of discharges were used alternatingly. One type of discharges was intended to shed light on the Fuchs effect while the focus in the others was the analysis of RF induced plasma rotation. In the former, the ICRF power was modulated throughout the flat-top of the discharge and a modulation frequency of 4Hz was used. In the latter, beam blips with a duration of 100ms were used to assess the toroidal and poloidal bulk plasma rotation. For the first and last blip the injected D particles have an energy of 130keV, while for the other blips the particles have an energy of 88keV. As fast particles speed up the plasma by transferring their momentum through Coulomb collisions, the time intervals during which the diagnostic beam is fired are short compared to the flat top time. In between beam blips RF power modulation at 25Hz was applied. No H beam was available and thus a D beam was used. Hence it is necessary to assess how the ICRF power affects this D population.

The applied RF power level was typically ~4MW, brought back to half that value during slow modulation and to 15% of the maximal value during fast modulation. The 4Hz slow modulation allows studying the response both of the ion and of the electron temperature to the RF power level change. The electron temperature is obtained from Electron Cyclotron Emission, (ECE) while the ion temperature is obtained from charge exchange measurements. Also global signals (such as the diamagnetic energy or the plasma energy) can be studied. The charge exchange diagnostic beam is left on during the whole discharge during the first type of shots, while it is only on for very limited periods during the second type of shots. The 25Hz modulation is too fast to capture the ion dynamics and solely allows studying the electron response. In spite of this drawback, the fast modulation is extremely useful as it is not suffering from the effects of heat wave diffusion away from the heat source and thus allows a better understanding of how the actual (be it only electron) power deposition profile looks like.

The applied frequency is ~32MHz (strictly the 4 A2 antenna arrays are driven at slightly different frequencies, 32.07 and 32.5MHz) and the toroidal magnetic field on the geometric axis ($R_0 = 2.97$m) is $B_0 = 3.41$T. Dipole ($0\pi\ 0\pi$) phasing was used in low triangularity plasmas such that the last closed flux surface is as parallel as possible to the A2 antennas to optimize coupling. The modest auxiliary power input leaves the plasma in L-mode. For the chosen parameters the N = 1 ^{3}He cyclotron layer lies slightly (~0.24m) on the low field side of the plasma core while the N = 1 H cyclotron layer is outside the machine on the low field side. The cold N = 1 D layer lies on the high field side but ICRF heated D beam particles will absorb wave power at their Doppler shifted resonance layer, which is close to the plasma core.

Figure 1 shows the time evolution of several key variables of two discharges at different ^{3}He concentrations. The ^{3}He concentration is scanned from 1 to 4% in Pulse No: 79343 and from 3% to 12% in Pulse No: 79352 (Fig.1d). In both discharges the response of the radiated power (Fig.1b), the electron temperature (Fig.1g) and the MHD energy (Fig.1f) to the modulation of the ICRF

power (Fig.1a) is clearly visible while the electron density response is weaker and the response of the ion temperature (Fig.1h) is absent. Note that the RF system struggles to couple power at the start of Pulse No: 79352 and the end of Pulse No: 79343, when the ^{3}He concentration is about 5% in both shots. Also the electron temperature response to the RF modulation is correlated with the ^{3}He concentration in the same way, showing the typical periodic increase and decrease as a result of the two alternatingly applied power levels.

For the imposed ICRF power of 3-4MW, core temperatures of 3-4keV are reached by the electrons, and slightly less (2-3keV) by the ions. Except for the radiated power, all signals for Pulse No: 79352 increase for increasing ^{3}He concentration. For the temperatures it can be seen that the whole profile responds to the ^{3}He concentration (see Fig.2 and Fig.1d for the X[^{3}He] reference), the electron temperature showing a general lifting of the profile, while for the ions the central response is more pronounced. While the temperature gradually fades away towards the edge, the density has an edge pedestal of 1-1.5 10^{19}/m^3, and central values reaching 2 to 2.7 10^{19}/m^3, depending on the minority concentration and possibly the limited but finite beam fuelling (see Fig.3).

2.2. DEPENDENCE OF KEY QUANTITIES ON X[^{3}HE]

Looking in detail at the response of various signals, one can distinguish 3 different regimes as function of the ^{3}He concentration: a regime at low concentration (<1.8%) at which the RF heating is efficient, a regime at intermediate concentrations (1.8-5%) in which the RF performance is poor, and finally a good heating regime at ^{3}He concentrations beyond 6%. Modelling as well as fast ion particle evidence identifies the first as a minority heating scheme, and the second and third as mode conversion schemes.

Figure 4 depicts the diamagnetic energy (Fig.4c), the neutron rate (Fig.4b) and the core electron temperature (Fig.4d) as a function of the ^{3}He minority concentration for a number of data points at similar densities (Fig.4a) between 5.5 and 6x10^{19}/m^3. Both the diamagnetic energy and the electron temperature exhibit a maximum at low ^{3}He concentrations, and fall sharply when reaching the first mode conversion regime. Between 3 and 5% of ^{3}He, the overall performance is poor. It recovers and becomes even better than that at low concentrations in the second mode conversion regime. It is worthwhile to note that the minority heating regime at low concentrations is not accompanied by a noticeable neutron yield, but that this quantity rises pronouncedly in the second mode conversion regime.

The observed heating efficiency is not solely a consequence of the wave dynamics inside the plasma but is – at least partly – due to the antenna-plasma coupling. In Fig.5 it can be seen that in the ^{3}He concentration intervals in which good heating efficiency is observed the antenna resistance is high, and that it falls away when approaching X[^{3}He] of 3-6% from either side. This correlation with the concentration can directly be observed on the coupled RF power level and on the resistance of individual straps, respectively higher and more responding to the modulation at low X[^{3}He]~1-2% than at intermediate concentrations of 2-4%.

2.3. RESPONSE OF THE PLASMA TO RF POWER MODULATION

Studying the experimental ICRF power deposition profile is traditionally done by studying the electron and ion temperature response to a modulation of the RF power. Apart from the temperature, also other quantities such as the density and the radiated power respond to changes in the RF power level (for a detailed analysis, see [10]). Finally, some of the power is lost before it is ever thermalized and thus the specificities of the fast particle populations (e.g. the fast ion loss) need to be monitored to obtain a full picture of the RF heating dynamics.

Figure 6 gives a typical example of the temperature response to the RF power in the recent (^{3}He)-H mode conversion studies. The bottom right figure (Fig.6d) shows the strong electron temperature response to the ICRF power, the fast temperature increase and decrease in direct correlation to the – modulated - ICRF power level. The central ion temperature channels (Fig.6c) are rather noisy but do not – at least to the naked eye – reveal any response to the RF power (Fig.6.b); in the outer channels hints of ion response are observed. As the temperature does not only change under the influence of the ICRF power but also under the influence of NBI power, the NBI power was kept low and constant during the shot. A minimum of NBI power is necessary since the ion temperature is inferred from the charge exchange recombination diagnostic that relies on the presence of a fast ion particle subpopulation. The electron temperature increase just after t=5s is due to the (high energy) NBI beam blip used to diagnose the plasma rotation in the mode conversion shots. It can be seen that the RF generators do not succeed in modulating the power early in the discharge (5.5<t<6.5s) and that the maximum power level launched increases as a function of time the first few seconds after that. This behavior is a consequence of the dependence on X[^{3}He] of the efficiency with which the power can be coupled into and absorbed inside the plasma (Figs.6a and 5d-e).

As the electron temperature diagnostic has 96 and the ion temperature diagnostic has 12 channels covering all magnetic surfaces of the plasma, studying the response of all temperature channels to the launched RF power allows to determine the experimental power deposition profile. Figure 7 depicts the slow (4Hz) variation of the electron temperature at R~2.5m in part of the RF heated flat top phase of Pulse No: 79352. Superposed on the experimental data are 3 types of fits used to approximate the experimental data: the dashed line is the result of fast Fourier analysis, the dash-dotted line is the result of the usual Break-In-Slope (BIS) analysis, while the thick full line depicts the guess provided by an enhanced BIS method allowing to capture the exponential saturation of the signal due to the presence of local energy sink mechanisms such as transport, Coulomb collisions, The upgraded BIS fits the data best but all 3 the methods perform more or less equivalently. In Fig.8 the power density estimated from the temperature response (Fig.8a) in the interval between 7 and 8s is depicted for the same shot; the corresponding integrated power density is provided as well (Fig.8b). Both the ion and electron profiles have a broad deposition profile with a maximum in the center. Electron heating is clearly much more dominant than ion heating, the volume integrated electron power density being about a factor of 3-4 larger than the volume integrated ion power density; all analyzing methods yield similar results.

That the ^{3}He concentration is a key parameter in the examined shots is clearly seen in Fig. 9. Both at low (Fig.9a) and at high (Fig.9b) concentration the maximum absorbed power density shifts outward for increasing ^{3}He concentration; the modulation frequency is 25Hz rather than 4Hz now so the ion dynamics is not captured anymore. At low concentration the maximum moves out rapidly depending on the minority concentration (the minor radius position shifting from ρ_{max}~0.4m when X[^{3}He] = 2.5% to ρ_{max}~0.55m when X[^{3}He] = 3.3%), while at higher concentrations the position of the power density maximum seems to be less affected by the ^{3}He content of the plasma. At first sight the location of the maxima seems puzzling: the fast-moving maximum seems to disappear at higher concentrations, and a new maximum enters the picture. It will be shown further on that this seeming inconsistency is a result of the dependence of the mode conversion layer position on the composition of the plasma.

The above discussed results purely account for the plasma energy response resulting from temperature variations. As was observed in Fig.1, the density tends to respond to the RF modulation just as well. Whereas the overall conclusion that the electrons are more sensitive to the RF power than the ions is not modified, the provided absorbed power fractions should be crancked up by a factor ~10%, taking into account the density variation.

The results of the RF absorption efficiency analysis as a function of the ^{3}He concentration are summarized in Fig. 10. The full dots represent the absorption by the ions, electrons and the summed power obtained from analyzing the charge exchange and ECE temperature profiles. The total absorbed power efficiency obtained by performing a Fourier analysis on the global MHD energy, is depicted as diamonds. The two are in reasonable agreement, although the heating efficiency derived from the MHD energy tends to be somewhat higher than the heating efficiency derived using the profiles. Taking into account that e.g. the ion temperature signal is somewhat noisy, one possible explanation is that this difference is due to the intrinsic inaccuracy of the diagnostics. The difference may, however, even more simply be due to the fact that some physics aspects are not properly included: e.g. both the reconstituted electron and ion temperature tend to be asymmetric w.r.t. the magnetic axis, suggesting that effects such as trapping of non-thermalized populations should be taken into account. Particularly at lower concentrations (X[^{3}He]~1%), part of the power is expected to be lost to the ions. Also, the (bulk) temperatures do not account for the energy carried by fast subpopulations. Globally, the absorption efficiency is 60-70% so the plasma can be heated efficiently in mode conversion scenarios. The fate of the remaining power is outside the scope of the present paper. It should be reminded, for example, that only the temperature and not the density variations were accounted for when computing the *local* power absorption at various radial locations, while a density response to the modulation of the ICRH power can clearly be observed at low concentrations in Fig.1; detailed information on the local density response is not available on the same time scale as the ECE data but the observed variations of the available density channels suggest that adding the density response would add an extra 10-15%. Also the absorbed power is normalized to the launched power and not to the net power available after subtracting the impact

of radiation; normalizing to the net available power would add another ~15%. Edge effects such as collisional absorption, non-resonant absorption and recycling due to fast particles intercepting the wall are likely to be responsible for some of the absorption efficiency differences and should strictly be included to more rigorously assess the missing power (see e.g. [10]). Finally, the points plotted in Fig.10 result from Fourier analysis of the temperature response to the RF power modulation. As this data is only accounting for the dominant term in the Fourier spectrum but not the full response, the data are likely to somewhat underestimate the actual heating efficiency.

Figure 10 reveals that there are several distinct heating regimes as a function of the ^{3}He concentration. At low ^{3}He concentration the heating efficiency grows as a function of X[^{3}He] up to X[^{3}He]~2-2.5%. In this region the MHD energy results (diamonds) indicate a higher heating efficiency than the results derived from the detailed profile analysis. Beyond the maximum at X[^{3}He]~2%, the heating efficiency degrades quickly. In this region the MHD energy and detailed profile analysis results totally corroborate one another. In the X[^{3}He] region from 4-6%, no trustworthy data could be obtained since the ICRF generators are struggling to couple power into the plasma, rendering the BIS/FFT analysis impossible. Noting that the antenna resistance drops down significantly in this region (see Fig.5), the reason for this 'void' is suspected to be related to wave propagation and/or damping and will be discussed later on in this paper. When reaching X[^{3}He]>6%, the heating efficiency has fully recovered and is – apart from a weak tendency of the electron and total heating efficiency - essentially independent of the minority concentration. Whereas the behavior at low concentration is fully in agreement with what would be expected from the Fuchs et al. constructive/destructive interference effect, the behavior at the higher concentration is at odds with it. To understand this aspect of the experimental findings it was necessary to go beyond Fuchs' model (see Section III).

One aspect to keep in mind when interpreting the plasma response to RF power modulation is that the temperature profile is shaped not only by the power sources but equally by the power losses. In Fig. 11 the power deposition profile is given for 2 time intervals in different shots with different modulation frequencies but with the same ^{3}He minority concentration of 3% and as identical as possible plasma and machine parameters. Both profiles exhibit a power density maximum close to the plasma core, and share the same location of the power density maximum at R~3.5m. But in spite of the similar conditions, the two power deposition profiles are markedly different, the profile at 25Hz being much more peaked than that at 4Hz. The former has a power density maximum of ~0.006MW/m^3 per MW launched while the latter 's peak is almost 3 times higher. Also the integrated electron power is significantly different: for slow modulation at 4Hz only 25% of the power is found back in the electrons, while 50% is recovered when $f_{mod} = 25$Hz. As the parameters have been chosen to be identical, the main effect that sets these 2 results apart is the diffusion of heat across the magnetic surfaces, and ultimately out of the plasma. When the modulation is fast, the temperature response mimics the deposition profile. But as heat diffuses away from the location at which it was deposited, slow modulation tends to yield broader and lower deposition profiles than

rapid modulation. Transport also carries heat across the plasma boundary causing a fraction of the power to be missing; part of the absorbed power may also go unnoticed because the line-of-sight of the JET ECE diagnostic is ~20cm below the actual magnetic axis, thus creating a 'hole' in the data for the plasma core. Finally - and recalling that the radiated power is a sensitive function of the ICRF power in the plasmas studied here - some of the power is radiated away from the plasma in the form of Bremsstrahlung and/or impurity radiation. As the average fraction of the power radiated away can be as high as 25-50% (see Fig. 1), the effective power available for heating the plasma is often significantly lower than the power launched. Although this realization does not make the heating scenario more efficient, it at least suggests that little power is lost through unidentified channels.

2.4. MULTIPLE MODE CONVERSION: SENSITIVITY OF THE POWER DENSITY ON THE PLASMA COMPOSITION

Since the position of the mode conversion layer critically depends on the plasma composition, a real time control scheme has been implemented in JET to impose a given value for the minority concentration in the experiments. The real time control scheme relies on a simple formula to estimate the ^{3}He concentration and adopts a PID (Proportional Integral Derivative controller) scheme to open the gas injection module whenever the measured concentration falls short of the wanted one. The ^{3}He concentration estimate is based on a formula – originally due to Mantsinen [11] – that links relative divertor light intensities of species to relative concentrations. Although this scheme is crude and incapable to make an accurate guess of the actual ^{3}He concentration in the plasma, it is sufficiently accurate to allow steering the minority gas injection module. Post-processing based on charge exchange spectroscopy data allows to link the crude data – strictly only locally relevant in the divertor – to the actual value at the mode conversion location.

Mantsinen reasoned that if the effective charge is known, if charge neutrality holds and if Carbon is the only impurity in the plasma, there is a simple formula to estimate the ^{3}He concentration:

$$\begin{aligned} 1 &= X_D + 2X_{^3He} + X_C 6 \\ Z_{eff} &= X_D + 4X_{^3He} + X_C 36 \end{aligned} \quad \rightarrow \quad X_{^3He} = \frac{6 - Z_{eff}}{5X_D / X_{^3He} + 8} = \frac{6 - Z_{eff}}{0.9\dfrac{DAO}{HE1O} + 8}$$

When, following a simple estimate from atomic physics [12], the relative concentrations X_D and $X_{^3He}$ are linked to the relative light intensities of the species (labeled as DAO and HE1O), this expression yields an easy guess for the ^{3}He concentration (strictly for the He concentration since the spectral lines of ^{3}He and ^{4}He are indistinguishable in practice). This expression was used for many L-mode experiments but proved to be inaccurate in H-mode and even more exotic (e.g. ITB) plasmas. Supplementing the experimental data with impurity light intensities but adopting the same philosophy as proposed by Mantsinen yielded a sufficiently accurate generalization of the original formula. Having found a guess for the ^{3}He concentration, all other concentrations can be estimated.

Because of the C wall tiles, JET plasmas typically contain 1-2% of Carbon. Additionally, D being the machine's most commonly used working gas and the fact that the reported experiments were performed after a ^{4}He plasma campaign, Deuterons and ^{4}He ions released from the wall by recycling were present in all discharges. Due to the use of diagnostic D beams, the concentration of D ions (and possibly ^{4}He ions due to the NBI duct 'contamination' resulting from a recent change-over from D to ^{4}He beams) was further enhanced. As the location of the ion-ion hybrid layers depends on the plasma composition, experimentally found mode conversion absorption positions can be correlated to the species' concentrations via a dispersion equation study.

A minimization was performed to estimate the actual plasma composition consistent with the experimentally determined power deposition data. The various plasmas concentrations were taken as free parameters in the minimization. Starting from an initial guess for the plasma composition, the experimentally found mode conversion positions (up to a small shift with respect to the position of the fast wave confluence because the damping on the mode converted branch only becomes efficient a small distance away from the confluence after it has modified its **k**-vector sufficiently to guarantee efficient damping) were identified with the confluence locations provided by a cold plasma root finder. It was found that the presence of small quantities of C, D and ^{4}He in the plasma – in addition to the injected ^{3}He - gave rise to a supplementary mode conversion layer close to the plasma center and hidden in the ECE data (recall that the ECE diagnostic at JET has a line of sight that is ~0.2m under the actual magnetic axis). Returning back to Fig.9 for a moment, it can now be stated more firmly that the central maximum in absorption in Fig.9a is due to mode conversion and not due to fast wave electron damping. Modelling done using density and temperature profiles that approximate the experimental ones further confirm this: for the chosen parameters, fast wave electron Landau damping and transit time magnetic pumping is very inefficient.

As all D-like species play a similar role from the ICRF heating point of view (the cyclotron frequency being proportional to Z/A), it is difficult to discriminate between the various D-like components. Although the average experimental curves could easily be identified with the corresponding confluence positions, the slope of the experimental data as a function of the ^{3}He concentration could not be matched, while the required D-like concentrations seemed excessive and outside the physically acceptable range. Realizing that the ^{3}He concentration used here as a reference is the guess obtained from the real time control formula (lacking e.g. profile information), it seemed plausible that a corrective factor should be applied to link the estimated ^{3}He concentration with the actual one. A multiplicative correction factor of 1.6 is found via the minimization (the corresponding figure with experimental and guessed concentrations is given in Fig.12). The obtained multiplicative factor corrects for the fact that the light intensity is not only a function of the concentration of the examined species but equally of the ambient temperature and electron density. Furthermore, one of the signals in the real time control guess being the relative light intensity of hydrogen and its isotopes, a small error in X[H]/(X[H]+X[D]) – typically of the order of a few percent in D majority plasmas but of order 1 now that H rather than D is the majority gas - can possibly also partially explain the

need for a corrective factor. Preliminary charge-exchange recombination spectroscopy data of the ^{3}He profile provide a similar correction. Finally, the TOFOR neutron diagnostic allows providing a rough guess for the actual D-concentration by comparing the ratio of the beam-thermal and beam-beam neutron emission [13]. A lowish value of X[D]~5-7% found is in good agreement with the guess provided by the minimization analysis.

Although the adopted procedure provides a way to reconcile the various experimental data, it is regrettable that there is no direct information available on the plasma composition and the individual species' density profiles.

2.5. RF INDUCED FAST PARTICLE POPULATIONS

Many ion heating scenarios are based on the capacity of ICRF waves to accelerate ions to high energies and deform the particle distributions well away from that of a thermalized population. JET has a number of diagnostics that allow monitoring the fast particles, either directly (as is the case for the fast lost ion collector [14] and neutral particle analyzer [15]) or indirectly (as is the case for the gamma ray spectrometers [14] or the time of flight neutron diagnostic [16]).

A first hint that fast particles were created in the (^{3}He)-H mode conversion experiments is given in Fig. 13. In the top right figure the neutron rate is depicted for 2 shots, Pulse No: 79347 with a ^{3}He concentration scan at modest concentrations and Pulse No: 79349 with ^{3}He concentrations increasing from ~2.5% and to ~12.5% (see Fig.13b). Although the average ICRF power level is lower for most of the time in the discharge with the highest X[^{3}He], the relative neutron rate is significantly different. Both neutron rate curves show a very similar behavior early in the shot (including the response to the earlier mentioned initial 130keV NBI blip used to assess rotation in the mode conversion shots) when their ^{3}He concentrations are similar but diverge gradually more as the difference in the ^{3}He concentrations become larger. The signature of the ICRF modulation is evident in the high concentration shot but is totally absent in the low concentration one. The already mentioned correlation between the coupled power and the ^{3}He concentration is noticeable here as well: when X[^{3}He] is about 3%, the maximum of the launched wave power is ~4MW, but when the concentration rises further to ~4%, there is a strong decrease in the maximal power launched.

Aside from the neutron rate, gamma ray spectroscopy (with both vertical and horizontal spectrometers) shows a very different pattern for the 2 shots: whereas in sPulse No: 79347 no high energy gamma rays are observed, two peaks stand out distinctly in the spectrum of Pulse No: 79349. The 2 maxima are the signature of threshold nuclear reactions necessitating the presence of fast ions for their occurrence. The peak at 4.4MeV corresponds to the ^{9}Be(α,nγ)^{11}B reaction and telltales the presence of a highly energetic ^{4}He subpopulation, while the peak at 3.1MeV is due to the ^{12}C(D,pγ)^{13}C reaction which requires fast D ions of at least 0.5MeV. The origin of the fast ^{4}He ions is likely *not directly* RF related i.e. they are not thought to be RF heated ^{4}He ions recycled from the wall. Rather, moderately fast RF heated D beam ions colliding with ^{3}He trigger the D(^{3}He,p)^{4}He reaction forming 3.6MeV α-particles and 15MeV protons; in the range of effective (D) temperatures

of 200-400keV, this reaction has a cross-section that is about 4 times higher than the D(D,n)^{3}He reaction. The fact that reasonably fast D is present is also inferred from evidence that the D(^{3}He,γ)^{5}Li branching reaction is taking place at high ^{3}He concentrations: This reaction gives rise to a broad spectrum of gamma rays with energies between 11 and 17MeV; for more details both on the fast ^{3}He as on the fast D and ^{4}He subpopulations in the presently studied scenario, see [14].

At very low ^{3}He concentration, the fast ion loss detector observes very energetic ^{3}He ions (see further). Whereas such a population could somehow be expected in a scenario tuned to central minority ^{3}He fundamental cyclotron ICRF heating, the D peak at higher ^{3}He concentrations is more surprising at first sight as one expects mode conversion heating rather than ion heating to be the dominant wave energy absorption channel. Similar evidence was, however, already presented in (^{3}He)-D plasmas equally tuned to ^{3}He N = 1 heating but in which the NBI D beam was observed to absorb a non-negligible fraction of the RF power at the Doppler-shifted D cyclotron layer [2]. Whereas the exact role of the bulk deuterons was not fully evident in the (^{3}He)-D experiments, the present (^{3}He)-H experiments make it clear – no dominant fraction of thermal D being present in this H-majority plasma – that the earlier observed phenomena are indeed solely due to the D *beam* ions. Also in the recent experiments a sufficiently *large* ^{3}He concentration was the key to triggering the formation of an ICRF heated D population. Figure 14 shows the neutron spectrum provided by the TOFOR (time-of-flight) detector: Whereas at modest X[^{3}He] no fast D tail is observed, a D tail with an estimated effective temperature of 250keV was present in high X[^{3}He] shots; as TOFOR relies on the time it takes secondary neutrons to travel between 2 diagnostic plates the independent variable in the plot is the time-of-flight, which is inversely proportional to the velocity of the particle so that the signature of high energy tail is visible in the left of the figure. The neutrons TOFOR detects arise from the DD nuclear reaction. Where D was the majority plasma in the earlier (^{3}He)-D experiments so that beam-target DD reactions were abundant, D is a minority in the present (^{3}He)-H plasmas so beam-beam reactions dominate.

JET is equipped with a scintillator probe fast ion loss detector [14], which detects ions with gyroradii from 0.03 up to 0.14m, and equally determines the particles' pitch angle. Fast ^{3}He ions with energies of 1.1MeV at a pitch angle of about 70^o were observed in the shots with finite but small ^{3}He content (see Fig.15). Tracing back the orbits of these particles to where they obtained their acceleration places them just off the ^{3}He resonance, identifying them as trapped particles with an essentially tangent resonance. The losses diminish when X[^{3}He] goes beyond 2.5%. There is a clear correlation between the gamma ray spectrum and the fast ion loss detector signal: in absence of fast ^{3}He or D ions in Pulse No: 79347, the 4.4MeV peak in the γ-ray spectrum disappears and only the 3.1MeV peak survives.

The scintillator probe equally detected fast D and ^{4}He particles. In shot # 79349 in which the ^{3}He concentration was about 10%, 1.1MeV D and 2.1MeV ^{4}He were observed early in the discharge while energies up to 1.8MeV for D and 3.9MeV for ^{4}He were reached later on. The pitch angle of the fast D and ^{4}He was about 57^o. The presence of fast ^{4}He was also inferred from the 4.44MeV

γ-ray peak of the $^{9}Be(\alpha,n\gamma)^{12}C$ reaction, while the 3.1MeV $^{12}C(D,p\gamma)^{13}C$ γ-peak revealed the presence of fast D. These 2 reactions are threshold reactions, requiring ^{4}He of at least 1.5MeV and D of at least 0.5MeV respectively. In shot 79352, RF modulation was used throughout the flat top and a ^{3}He concentration scan from 2% to 12% was performed. The modulation of the RF power can clearly be seen in the fast D and ^{4}He particles losses when $X[^{3}He]>6\%$. A loss in RF power is also immediately detected via a drop in the γ-ray signal.

2.6. A SHORT NOTE ON INTRINSIC AND RF INDUCED ROTATION

As mentioned at the outset, the rotation analysis was done using dedicated shots designed to ease the rotation analysis. Although rotation analysis is not the main topic of this paper, some key results of these experiments are briefly sketched here. For more information, both on the rotation experiments themselves and their interpretation, see [17]. Poloidal and toroidal plasma flow is typically observed relying on charge exchange analysis. As charge exchange relies on a fast ion (beam) population, the analysis of the rotation is somewhat delicate as the diagnostic beam itself transfers its momentum to the plasma and causes it to rotate. On the other hand waiting some time after the beam switch-on is needed to ensure that a sufficient amount of charge exchange events occur and that the required equilibration has set in. The former reason is responsible for the fact that rotation analysis is done using beam blips (in the present case of 100ms, data being taken every 10ms) rather than sustained beam injection. The latter necessitates discarding the first data point in the analysis. The results shown are the average of the 2^{nd}, 3^{rd} and 4^{th} data point after the switch-on of the diagnostic beam; various beam blips are spread over the discharge. To have an idea of the power deposition profile, 25Hz modulation intervals are interspersed in between the diagnostic beam blips.

Figures 16a&b show the poloidal and toroidal rotation profiles observed for several values of $X[^{3}He]$. In the absence of RF heating as well as at low ^{3}He concentration, the plasma column is co-rotating poloidally. Increasing the ^{3}He concentration results in a central counter-rotating flow. The whole plasma is participates in this flow, up to the plasma edge, as can be seen from the reduction in co-rotation of the outer plasma zones. The highest counter-rotation velocities are observed at the highest ^{3}He concentrations. Central counter-rotation values of up to 6krad/s are reached.

Together with toroidal rotation, poloidal rotation is observed. Similar to the toroidal rotation, the poloidal rotation increases at higher ^{3}He concentration with increases in the poloidal rotation of up to 10km/s.

Figure 16c&d depicts the toroidal and poloidal rotation as a function of the ^{3}He concentration. Whereas the edge rotation simply decreases linearly with the ^{3}He concentration, the magnitude of the central toroidal rotation seems to exhibit a maximum at about $X[^{3}He] = 4\%$ and a minimum at 7%. At the highest concentration reached in the experiments ($X[^{3}He] = 12\%$) the rotation velocity reached about 8krad/s. The dependence of the rotation velocity on the minority concentration is somewhat ambiguous in Fig.16 since the ICRF power level was not identical throughout the scan, although this is indirectly a consequence of the minority concentration as well. Renormalizing

the data by the relevant ICRF power level (yielding an almost linear curve) is not yielding a more representative answer either since the rotation is composed of an intrinsic component and an ICRF induced one; ideally one would need to subtract the intrinsic part and renormalize the RF induced part only to have an idea of the amount of rotation driven by each MW of ICRF power but as the data of the intrinsic rotation at the temperature and density reached for each ^{3}He concentration are not known, it is impossible to disentangle the two effects.

3. MODELLING

Since the short wavelength ion Bernstein or ion cyclotron branch is excited by the fast wave in virtually all ICRF heating scenarios – more or less efficiently depending on the parameters chosen - and since the mode conversion layer lies very close to the ion cyclotron layer so that it is not always possible to disentangle conversion and damping dynamics, the study of the physics of mode conversion is crucial to get a good grip on the interplay between the waves and the way their cross-talk can be enhanced or avoided. Whereas most works focus on the derivation and exploitation of an as complete as possible model (see e.g. [18-22]), it is interesting to take a step back and try to understand the basics of wave confluence using a purely analytical description. Obviously lacking some details and thus inappropriate to make actual predictions, such description nevertheless helps building the intuition needed to understand the observed wave dynamics.

Figure 17 depicts a qualitative picture of how mode conversion of two waves can be understood, starting from the dispersion root diagram of the modes in question. Considering the interaction region of the waves as a black box, a wave with unity incoming flux and impinging on that box from the left will partly transmit (T) and – assuming damping is absent in the model - will transfer the remainder of its energy (1-T) to the other wave. Systematically following the various daughter-waves created from the original wave using this elementary 'black box' reasoning then easily yields reflection, transmission and mode conversion coefficients. Although 'tracing' the waves in such a way seems crude, it turns out to be powerful: For the case of the tunneling equation, analytical expressions for the connection coefficients are available. They confirm the above intuitive results, providing a rigorous mathematical backing for it [23].

Fuchs [1] noted that a fast wave excited at the low field side proceeds to its high field side cutoff in the low density region after it has gone through the mode conversion region where it locally excited a short wavelength branch. Hence a finite amount of wave energy is re-incident on the conversion region, this time from the high field side. Fuchs analytically determined the connection coefficients for that situation, adding an extra cutoff on the right of the drawing in Fig. 17. He found that the above simple reasoning can be used to predict the generalized connection coefficients, up to one ingredient: As waves have a phase, the evolution of this phase needs to be properly tracked in case of multiple incidences of a wave on the same conversion layer. Whereas re-applying the earlier reasoning for the second encounter separately one would find that the total connection coefficient

resulting from the 2 encounters is simply doubled from T(1-T) to 2T(1-T), the more rigorous result turns out to be $2T(1-T)(1+\sin\alpha)$ where $\alpha=2\Phi+\Psi$ is the phase of the total reflected wave with Φ the wave phase difference between the confluence point and the high field side cutoff and Ψ the phase of the reflected wave on the low field side. Note that the mode conversion coefficient can now reach any value between 0 and 1 provided the parameters are chosen such that T reaches its maximal value, 1/2. Tuning the plasma parameters appropriately thus allows a significant increase of the energy ultimately damped on the short wavelength branches.

Kazakov [4] took the Fuchs reasoning a step further and included a second mode conversion layer and its associated cutoff. Relying on the phase integral method he found that the total mode conversion coefficient becomes $T_1T_2\,(1-T_1T_2) + 4T_2\,(1-T_2)(1-T_1)\sin^2\alpha/2$ in which T_1 and T_2 are the transmission coefficients through the individual evanescence layers and located closer to the high and low field sides, respectively. The interference term involving the angle $\alpha=2\Phi + \Psi_2-\Psi_1$ mostly depends on the distance between the conversion layers.

Figure 18 qualitatively depicts the change of the power lost from the externally excited fast wave through a simple confluence mock-up model

$$d^2E/dx^2 + k^2(x)\,E = 0$$

in which the confluences have been substituted for quasi-resonances, with

$$k^2(x)=k^2_{ref}(\mathrm{atan}(\beta[x-x_L])-\mathrm{atan}(\beta[x_R-x]))2/\pi + C_1/(x - x_1 + i\,\nu) + C_2/(x - x_2 + i\,\nu).$$

In the above (see Fig.18a), aside from 2 locations - x_1 and x_2 - at which the wave has a (quasi-) resonance and a nearby cutoff, there are 2 supplementary cutoffs – at $x_{L(eft)}$ and $x_{R(ight)}$ - isolated from the others and representing the outer fast wave cutoffs ($k_o^2R_{Stix} = k_{//}^2$) in the low density region. Due to local absorption at the quasi-resonances x_1 and x_2, the wave flux jumps at these locations, as shown in Fig.18b for various positions of x_2. When both resonances lie inside the integration domain, the total absorption is the sum of the 2 localized contributions; it is a sensitive, oscillating function of the actual value of x_2. When x_2 is outside the domain of interest, not only the corresponding absorption drops to zero but also absorption at x_1 is varying less. Including the low field side fast wave cutoff x_R in the model reveals a supplementary feature the ICRF launching system needs to cope with: prior to becoming propagative the wave then needs to tunnel through an evanescence region.

Both the Fuchs and Kazakov expressions show that the constructive/destructive interference of the various waves critically depends on the relative position of the various confluence and cutoff layers. For the case of Alfvén heating this effect was noted by Karney et al. [24]. A similar effect – upon accounting for the wave reflection from the metallic wall of the vessel – was found by Heikkinen et al. [25]. Assessing – via dispersion equation root studies - how the cutoff and confluence

positions move as a function of tunable parameters as e.g. the density, the minority concentration, the dominant modes in the antenna spectrum and the magnetic field is crucial for tuning the mode conversion scheme. As the ICRF power is mainly carried into the plasma by the fast magneto-sonic wave, a few illustrations are given in this section of the sensitivity of the fast wave dispersion root to such tunable parameters.

Figure 19 represents a typical fast wave dispersion for the recent (^{3}He)-H experiments in JET. The magnetic field and frequency considered are $B_0 = 3.41$T and f = 32.35MHz, placing the ^{3}He cyclotron layer slightly on the low field side of the magnetic axis. Recall that (^{3}He)-H is a so-called 'inverted' scenario: whereas in a standard plasma the minority species has a charge-over-mass ratio that is bigger than that of the majority ions, the opposite is the case here. The consequence is that the ion-ion hybrid resonance moves towards the low rather than to the high field side for increasing minority concentrations and that it is encountered by the wave before the minority cyclotron layer is reached. As the figure depicts the fast wave dispersion root for a number of different ^{3}He concentrations, the sensitivity of the conversion/cutoff layer to X[^{3}He] is evident: a 1% change in X[^{3}He] results in a 0.06m change of the cutoff position.

It was mentioned that the plasma was contaminated with D-like particles (D, C, ^{4}He). These equally have an impact on the position of the confluence layer and hence on the deposition profile. Each 5% increase of the D concentration moves the fast wave cutoff 0.1m towards the low field side edge. Aside from the effect they have on the position of the conversion layer close to the antenna, the D-like species affect the wave fate in another important way by introducing a supplementary conversion layer. Just like the ^{3}He minority ions, the D ions form an inverted scenario population with the majority H, this second confluence layer shifts towards the *high* field side for increasing X[^{3}He] at constant concentration of the D-like species i.e. towards the low field side for fixed X[^{3}He] and increasing X[D]. The position of this layer is less sensitive to the ^{3}He changes than the one first discussed. Also the high field side cutoff is hardly budging when the concentrations are varied.

On the other hand, the high field cutoff position is a very sensitive function of the local parallel wave number (see Fig.20): changing the toroidal mode number by 10 moves this cutoff by 0.4m. The low field side and inner cutoffs are, in turn, much less sensitive to this parameter. And as the fast wave cutoff position in the low density region is not only a function of the edge density but also of the parallel wave number, one can easily show that the density profile factor as well as the edge density have a big impact on the position of the fast wave cutoffs.

The qualitative discussion of the impact of the position of the mode conversion and cutoff layers having been demonstrated qualitatively via the Fuchs and Kazakov formulae, and the dispersion study showing how these positions themselves critically depend on the plasma composition, some simulations of hot plasma wave propagation and damping are now discussed to get a firmer idea of the interplay of the various wave modes in the plasma.

The TOMCAT [22] 1D wave equation code has been used to analyse the wave propagation and damping dynamics of the (^{3}He)-H scenario. TOMCAT retains the toroidal curvature of the torus but

omits poloidal field effects. It is based on a variational formulation of the wave equation and relies on a finite Larmor radius expansion up to second order in the operator acting both on the electric field components and on the test function, yielding up to fourth order Larmor radius corrections and a description that retains up to dominant 3rd cyclotron harmonic heating terms and guarantees positive definite power absorption for both short and long wavelength, propagative or evanescent waves in the plasma. Except for the leftward propagating fast wave eigenvector, all waves able to carry energy into the integration domain of interest are imposed not to carry any energy. TOMCAT solves a 12th order equation yielding not only the local and global power balance to the various species but also all connection coefficients of the modes able to carry wave energy out of the domain of interest. On the high field side, the fast wave cutoff has been included in the considered interval while on the low field side the integration is started slightly inside the region where the fast wave is already propagative. Opposite to what is more standardly done – extending the integration interval up to the metallic walls of the vacuum vessel so that no wave power can enter nor escape - this procedure allows to assess the heating efficiency of an RF heating scenario as it predicts how much power is absorbed and how much is leaving the plasma after a full double sweep of the wave over the plasma.

Figure 21a shows the localized electron deposition profiles arising due to the 2 confluence layers, Fig. 21b depicts the dispersion equation roots and Fig.21c gives the corresponding parallel electric field component responsible for electron Landau damping. The ^{3}He cyclotron damping is taking place at x~0.2m but the ion heating is completely dwarfed by the electron heating. Short wavelength structure locally strongly enhances the electron damping (the net electron absorption being proportional to the perpendicular wave number squared) while the ion heating is inefficient as the component responsible for ion heating is small near the cyclotron layer but large near the confluence layers which are well separated from the Doppler widened region where cyclotron interaction would be possible.

Assuming the D, ^{4}He and C concentrations that are provided by the real time control formula are correct, and for the typical densities and temperatures experimentally observed, the heating efficiency for a number of toroidal mode numbers is shown in Fig.22. The oscillating character of the heating efficiency as a function of the minority concentration is the consequence of the constructive and destructive interference discussed by Fuchs and by Kazakov. Minority heating is significant only at low concentration while electron heating dominates the overall absorption. Depending on the antenna phasing chosen the cumulative effect of the various toroidal modes is different. Adding several modes tends to smooth out the oscillations at the modest concentrations. Since the heating efficiency of all the toroidal modes degrades when approaching the X[^{3}He] = 4%, one expects a marked decrease in heating efficiency when approaching that concentration independent of which phasing is chosen. At high X[^{3}He] the heating efficiency is markedly less dependent on the actual value of the concentration than it was at the lower concentrations. In between these 2 distinct regions there is a gap: just like the coupling is poor in that X[^{3}He] range in the experiment, the wave model suffers.

Qualitatively, the two types of behavior, as well as the changeover, are explained using the Fuchs conversion efficiency expression and the extension of it provided by Kazakov: The sensitivity due to the constructive/destructive interference caused by the presence of the multiple conversion layers and the fast wave cutoffs, the inability to couple power efficiently when a conversion layer blocks the waves penetrating the plasma, and the soothing effect of one of the conversion layers when lying behind the antenna.

Being a 1-D wave code and thus by definition lacking 2-D effects such as wave focusing, and missing a proper global description of the real geometry, TOMCAT's estimates need to be supplemented with those of a 2D wave code. Fig. 23 depicts the deposition profiles computed by the TORIC wave code [18] and overlays them with the experimental deposition profiles. Realizing that the experimental deposition profiles do not discriminate between heat directly absorbed by waves on a given magnetic surface and heat indirectly ending up on the electrons either via transport in physical space or by Coulomb relaxation of an energetic (D or ^{3}He) tail onto the electrons, a fair agreement between experimental and predicted data is obtained. The 2-D deposition profiles are broader than their 1-D equivalents largely for geometrical reasons since both the mode conversion and the cyclotron layers are located at R~constant and thus a given major radius position contributes to the energy deposited on various magnetic surfaces. Simply accounting for that "spreading" factor on the 1-D results yields the wing-like depositions with a sharp rise towards the core and a more shallow decrease towards the edge; the position at which the maximum absorption is reached is accurately being predicted by the 1-D wave equation solver, as can easily be seen glancing at Fig.21d depicting the 1D TOMCAT deposition profile as a function of the magnetic surface label ρ (= half the width of the magnetic surface in the equatorial plane). A more important issue missed entirely by the 1-D description is the fact that wave interference is somewhat moderated when the full geometry and wave sloshing over the vessel is accounted for, which tends to smoothen the deposition profiles and yields less pronounced interference patterns when summing over all (coupled) poloidal and (decouped) toroidal modes of the wave spectrum.

CONCLUSIONS

Recent mode conversion experiments in (^{3}He)-H JET plasmas allowed to identify the possibility to enhance the mode conversion efficiency by properly tuning the plasma parameters but equally demonstrated that such optimization becomes nontrivial when due to the presence of multiple ion species in the plasma multiple mode conversion layers simultaneously occur. The experiments also underlined that although some plasma constituents may themselves not be heated by the ICRF waves, they can have a considerable impact on the RF heating efficiency.

The heating efficiency at the various ^{3}He concentrations was found to be intimately related to the mode conversions layers residing in the plasma. At very low ^{3}He concentrations fast ^{3}He ions testify for efficient minority heating although bulk ion response was never observed to be significant. The electrons, however, react promptly to steps in the ICRF power level used to determine the

experimental power deposition profile. At ^{3}He concentrations of ~5%, poor ICRF coupling gave rise to poor heating performance. Analysis linked this reduced performance to a mode conversion layer crossing the low field side edge, a wide evanescence layer being present in front of the antenna, hindering wave to penetrate the plasma. At still higher concentrations, just 1 rather than 2 mode conversion layers lie inside the plasma. This results in increased heating efficiency, less sensitive to the actual ^{3}He concentration.

The different behavior in 2 various mode conversion regimes could be explained with the constructive/destructive interference scheme proposed by Fuchs [1] and its generalization to 2 resonance / mode conversion layers by Kazakov [4]. Provided the plasma constituents are well known, minute changes of the most relevant parameters (X[^{3}He], B_0, antenna phase) allow to tune the heating scheme to optimize the heating efficiency. The experiments discussed in this paper have, however, demonstrated that this tuning might not be straightforward if the interaction of the waves with the wall is not controlled: as already noticed by Mayoral [9], D-like ions have a non-negligible impact on the position of mode conversion layers in inverted scenarios.

The experimental heating efficiency varied from 0.3 to 0.7. Conform with theory, the electron response is much more prominent than the ion response. Subpopulations of fast particles were created: At very low ^{3}He concentration the signature of very fast ICRF accelerated ions was seen in the fast ion loss detector and the gamma ray detector. At high ^{3}He concentrations, fast ^{3}He particles were no longer observed but fast D and ^{4}He populations were detected by various diagnostics (in spite of the fact that electron heating is aimed at these high concentrations). The neutron rate – resulting from colliding ICRF heated D neutral beam particles – rose to a level of 10^{14} neutrons per second at high ^{3}He concentration while the neutrons are virtually absent at low ^{3}He concentration. ICRF heated D beam particles are accelerated to energies of ~250keV. The fast ^{4}He observed are likely not RF heated ^{4}He but α-particles arising from the nuclear reaction D(^{3}He,p)^{4}He.

ACKNOWLEDGEMENT

This work, supported by the European Communities under the contract of the Association between EURATOM and the Belgian State, was carried out within the framework of the European Fusion Development Agreement. The views and opinions expressed herein do not necessarily reflect those of the European Commission.

REFERENCES

[1]. V. Fuchs et al 1995 *Physics of Plasmas* **2** 1637–47

[2]. D. Van Eester et al, *Plasma Physics and Controlled Fusion* **51** (2009) 044007

[3]. D. Van Eester et al., "***Mode conversion heating in JET plasmas with multiple mode conversion layers***", 37th EPS Conference on Plasma Physics, Dublin (2010) paper P5.163

[4]. Ye. Kazakov et al., *Plasma Physics and Controlled Fusion Plasma Physics and Controlled Fusion* (2010) 115006

[5]. P. Mantica et al., *Physical Review Letters* **96,** 095002 (2006)

[6]. Y. Lin, '*ICRF mode conversion flow drive in JET D-(^{3}He) plasmas and comparison with results from Alcator C-Mod'*, 37th EPS Conference on Plasma Physics, Dublin (2010), paper P5.164

[7]. E. Lerche et al., "*Experimental investigation of ICRF heating scenarios for ITER's half–field phase performed in JET ",* 37th EPS Conference on Plasma Physics, Dublin (2010), *paper O4.121*

[8]. E. Lerche et al., "*Experimental investigation of ICRF heating scenarios for ITER's half-field Hydrogen phase performed in JET*", to appear in the same topical PPCF issue as the present paper

[9]. M.-L. Mayoral et al., *Nuclear Fusion* **46** (2006) S-550–S-563

[10]. Lerche et al., *Plasma Physics and Controlled Fusion* **50** (2008) 035003 (26pp)

[11]. M. Mantsinen et al., private communication

[12]. M. Stamp, private communication.

[13]. C. Hellesen et al. Review Scientific Instruments **81**, 10D337 (2010) and C. Hellesen, "*Diagnosing Fuel Ions in Fusion Plasmas using Neutron Emission Spectroscopy*", PhD thesis, Uppsala University, 2010 (http://www.diva-portal.org/smash/get/diva2:294070/FULLTEXT01)

[14]. V. Kiptily et al., "*Fast ions in mode conversion heating (^{3}He)-H plasma in JET*", submitted to PPCF to appear in the same topical PPCF issue as the present paper.

[15]. A.A. Korotkov *et al., Nucl. Fusion* **37** (1997) 35–51

[16]. M. Gatu Johnson et al. "The 2.5-MeV neutron time-of-flight spectrometer TOFOR for experiments at JET", *Nucl. Instr. Methods A* (2008) 591:417.

[17]. T. Hellsten et al., " *Evidence of torque due to electron heating in inverted mode conversion scenarios in JET*", to appear in the same topical PPCF issue as the present paper

[18]. M. Brambilla, *Plasma Phys. Control. Fusion* **41** (1999) 1

[19]. P.U. Lamalle, "*Nonlocal theoretical generalization and tridimensional study of the coupling of an ICRH antenna to a tokamak plasma*" (1994) *PhD Thesis LPP-ERM/KMS Report* 101, Université de Mons.

[20]. R.J. Dumont, *Nuclear Fusion* 49 (2009) 075033 (14pp)

[21]. M. Brambilla, *Nuclear Fusion* **28** (1988) 549.

[22]. D. Van Eester et al., *Plasma Physics and Controlled Fusion* **40** (1998) 1949–1975.

[23]. T.H. Stix, "*Waves in Plasmas*" (1992) AIP, New York, p. 510-513.

[24]. C.F.F. Karney, F.W. Perkins, Y.-C. Sun, *Physical Review Letter* **42** (1979) 1621–1624.

[25]. J.A. Heikkinen, T. Hellsten, M.J. Alava, *Nuclear Fusion* **31** (1979) 417–1624.

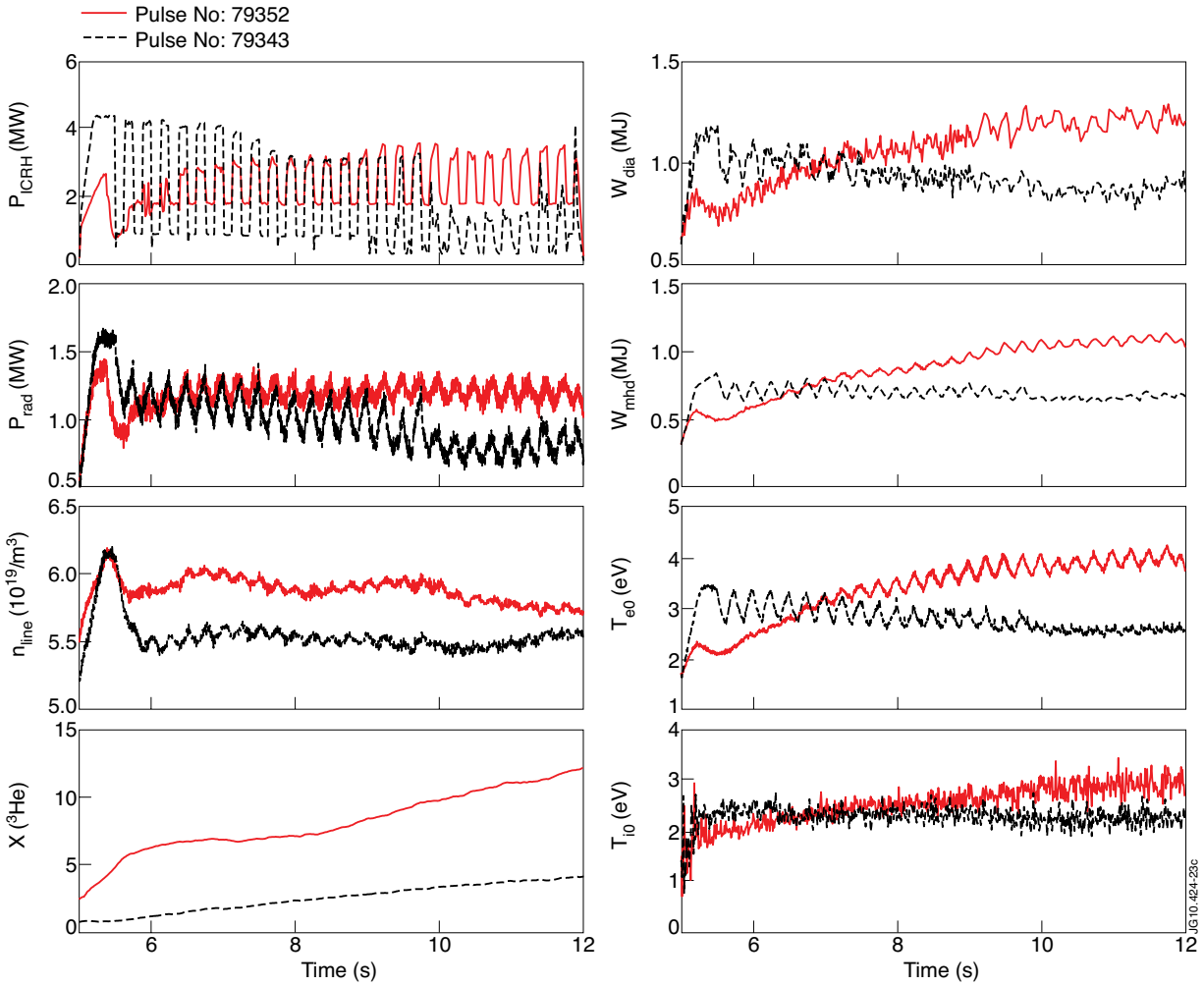

Figure 1: Overview of some characteristic quantities for Pulse No's: 79343 (with a modest X[3He] scan) and 79352 (in which 2.5%< X[^{3}He]<12%): (a) modulated ICRH power, (b) radiated power, (c) line integrated density for a chord through the plasma center, (d) real time control estimate of the ^{3}He concentration, (d) diamagnetic energy, (e) plasma energy, (g) central electron temperature and (h) central ion temperature.

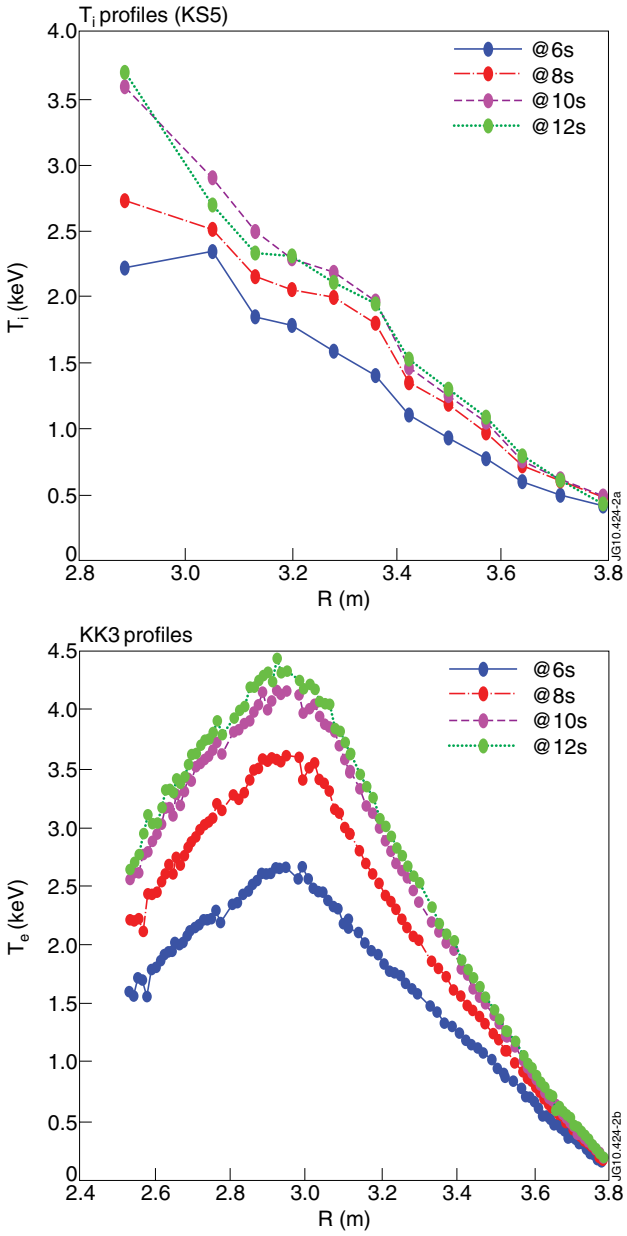

Figure 2: (a) Ion and (b) electron temperature profiles at various times and thus for various ^{3}He concentration during Pulse No: 79352 in which the minority concentration was scanned using real time controlled gas puffing (see Fig.1).

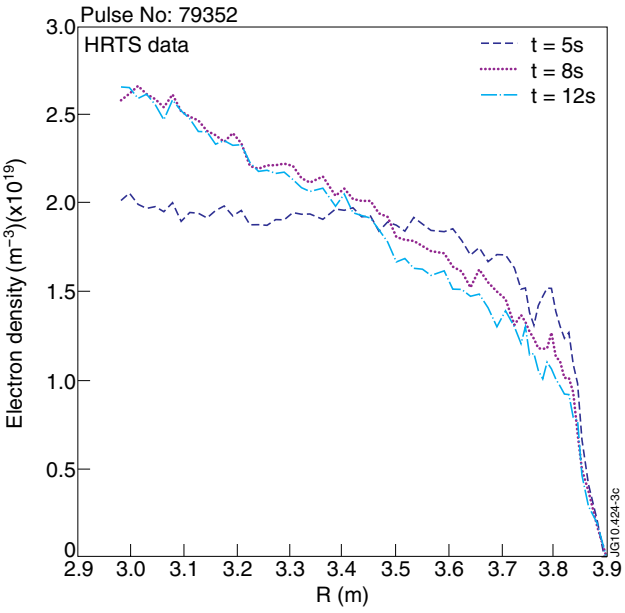

Figure 3: High resolution Thomson scattering density profile for Pulse No: 79352 at various instants.

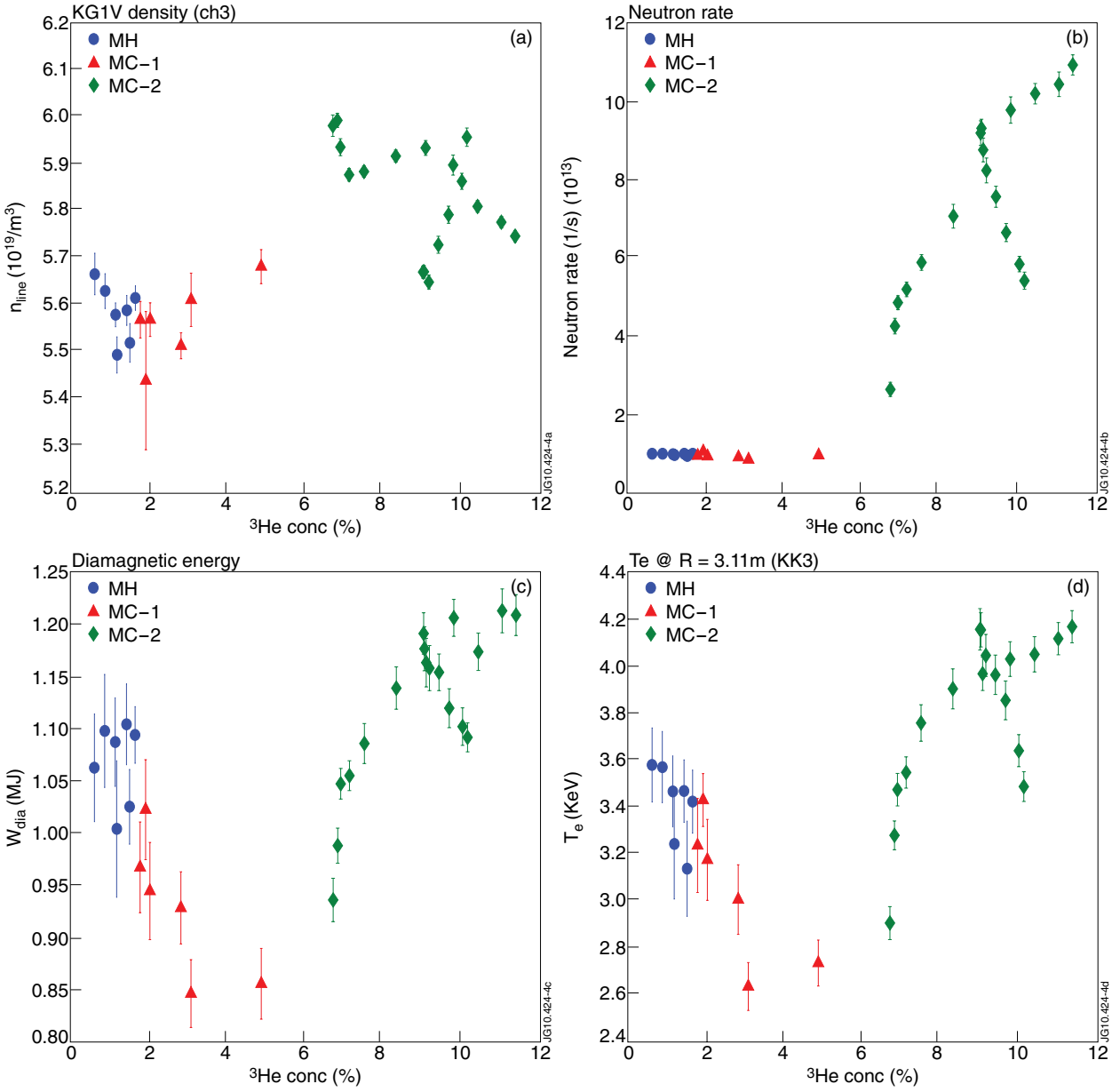

Figure 4: Summary plot over the full experimental session of various key quantities as a function of the $_3$He concentration: (a) line averaged density, (b) neutron rate, (c) diamagnetic energy and (d) electron temperature.

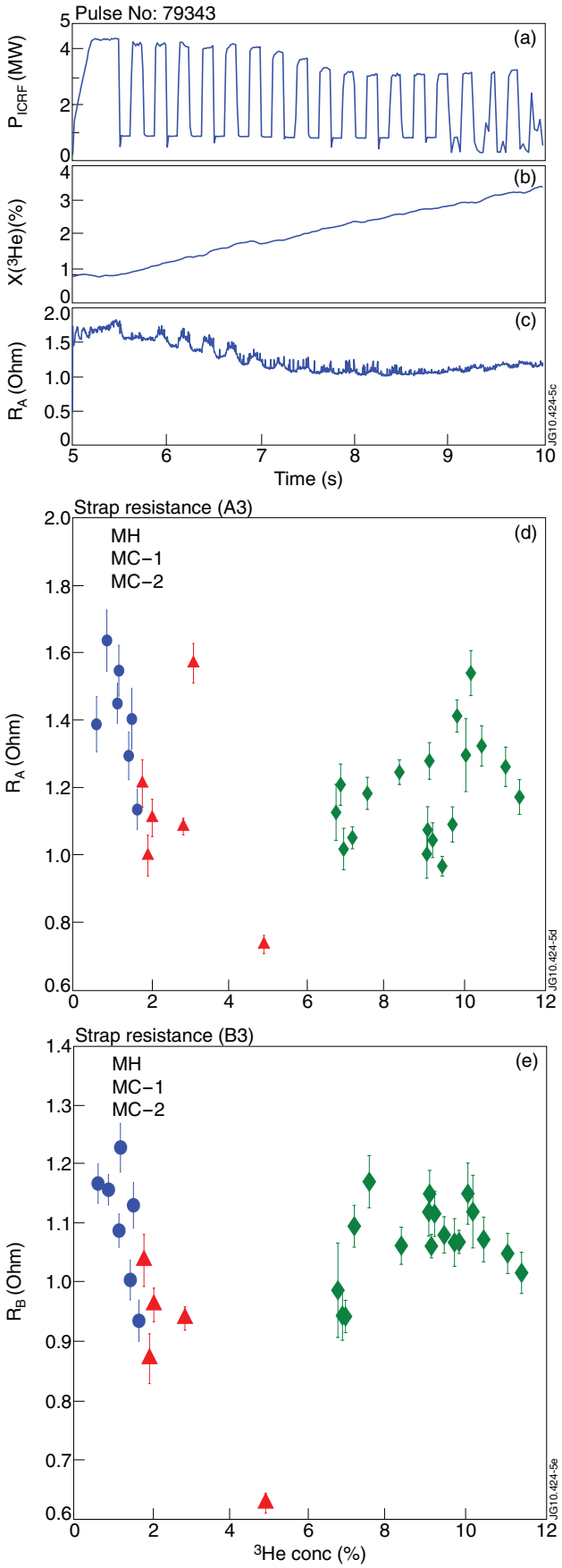

Figure 5: ICRF system performance as a function of time for Pulse No: 79343 (a-c) and as a function of the 3He concentration (d-e): (a) ICRF power level, (b) ^{3}He concentration, (c) resistance of the A3 strap of the JET A2 antenna as a function of time, (d) and (e) resistance of the A3 and B3 straps as a function of the ^{3}He concentration.

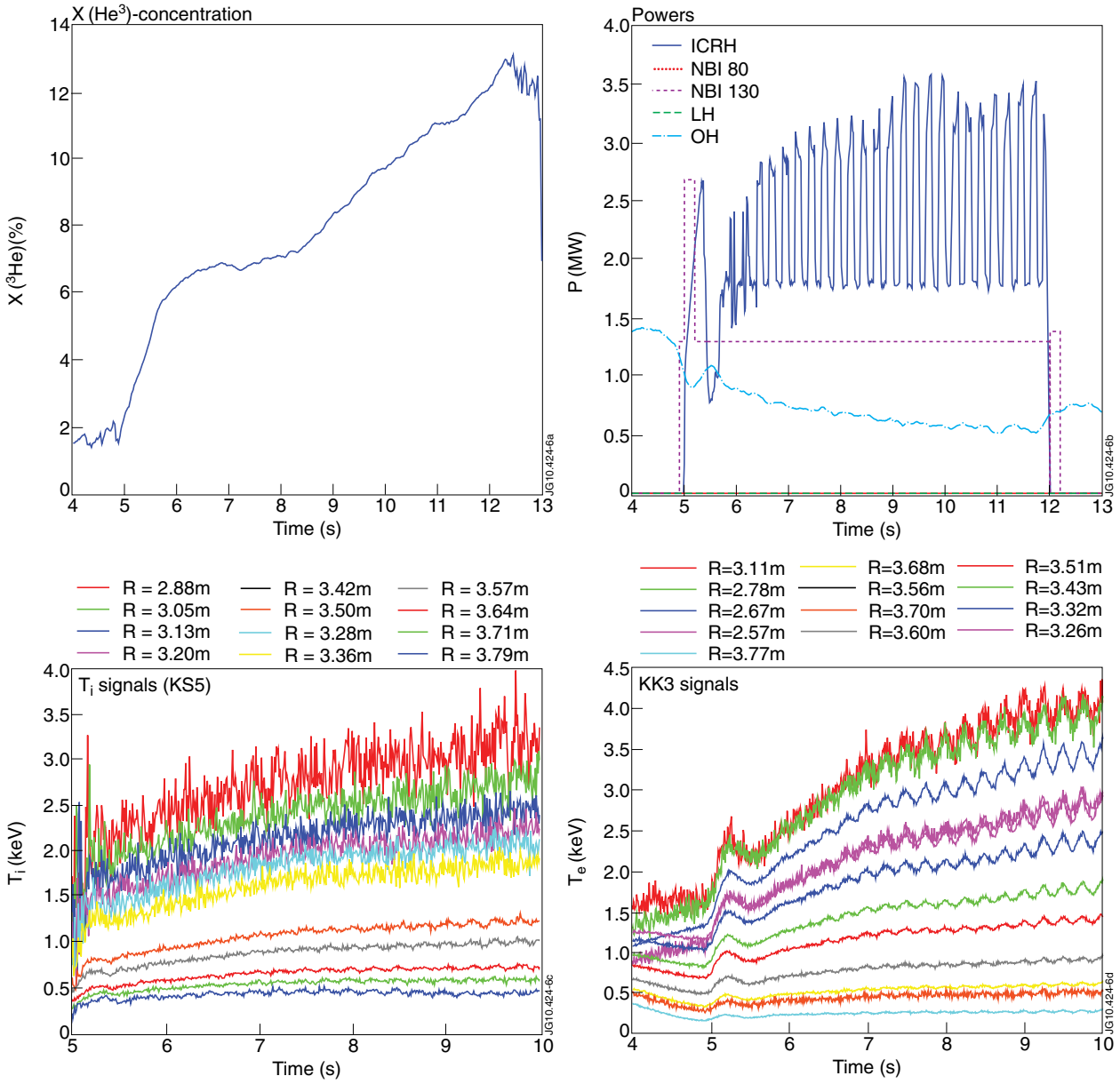

Figure 6: Temperature response to the auxiliary heating power for Pulse No: 79352: (a) ^{3}He concentration, (b) ICRF power level, (c) ion temperature, (d) electron temperature.

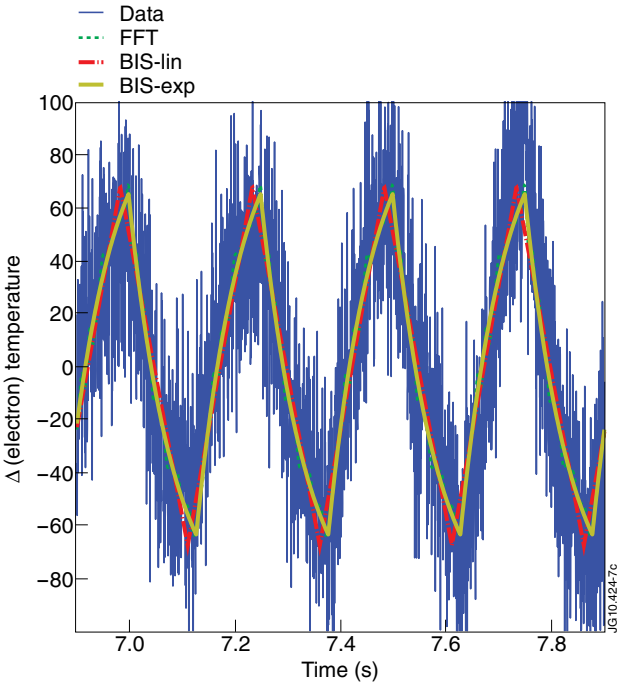

Figure 7: Close-up of the electron temperature variation inferred from the ECE diagnostic for Pulse No: 79352 at R~2.5m, and the fits found by Fast Fourier Transform, classical Break-In-Slope or enhanced Break-In-Slope analysis.

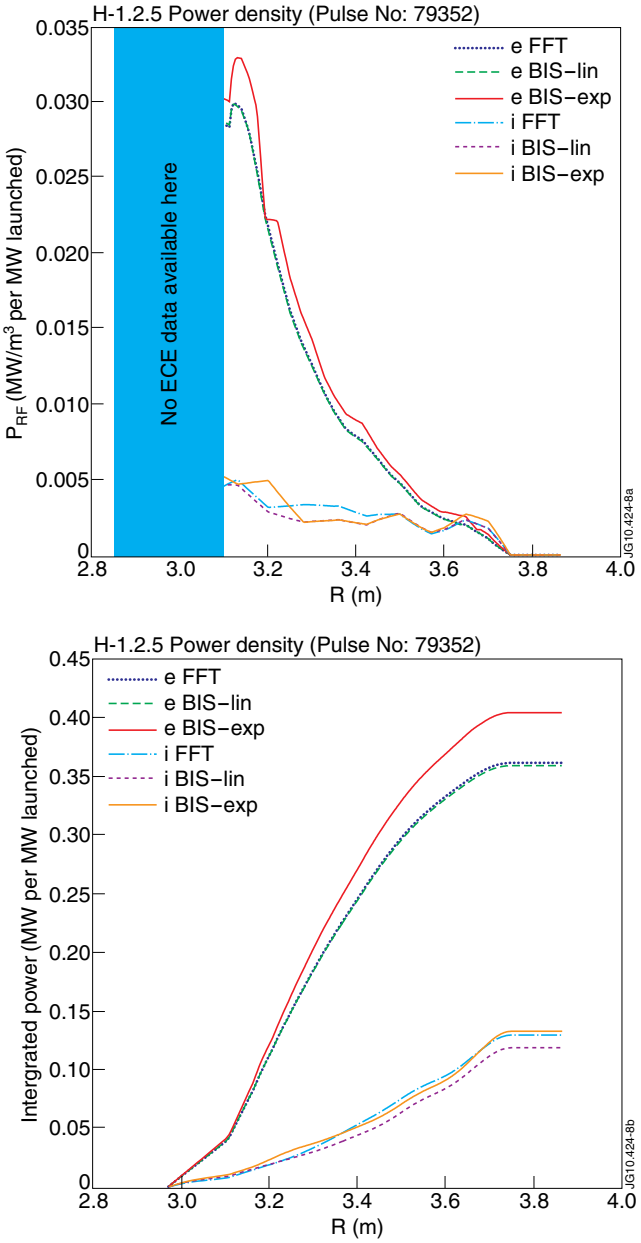

Figure 8: (a) electron and ion ICRF power deposition profile obtained by FFT or BIS analysis for Pulse No: 79352, and (b) volume integrated electron and ion power densities.

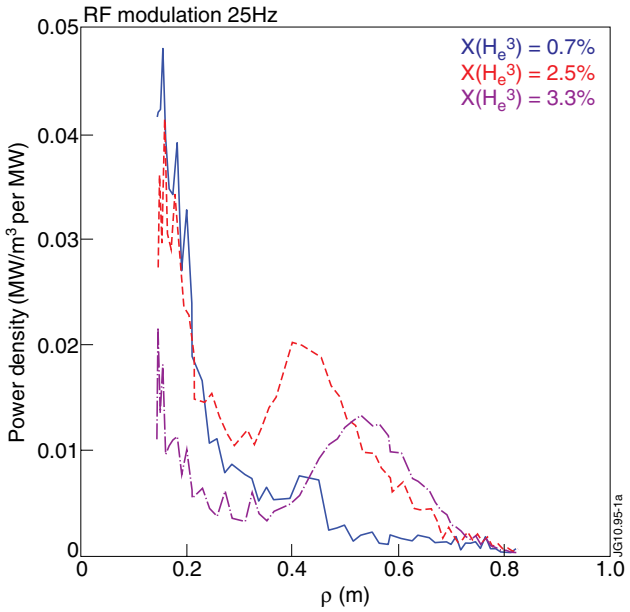

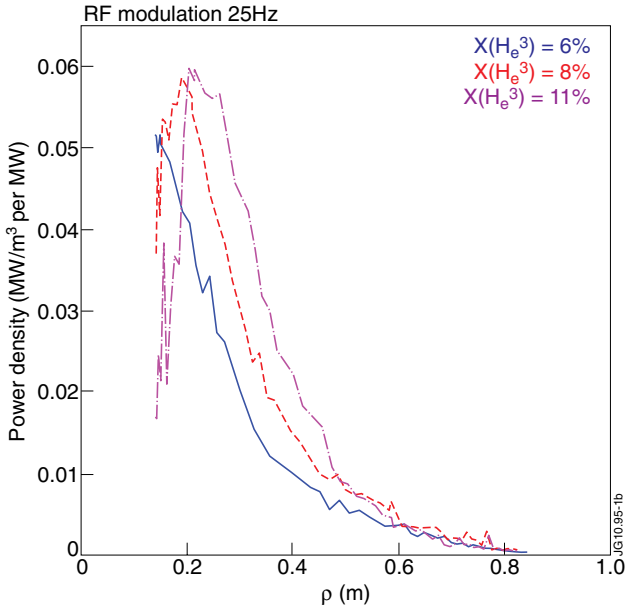

Figure 9: Electron power deposition profile for various 3He concentrations inferred from analysis of the electron temperature to a 25Hz modulation: (a) 0.7%, (b) 2.5%, (c) 3.3%, (d) 6%, (e) 8%, (f) 11%.

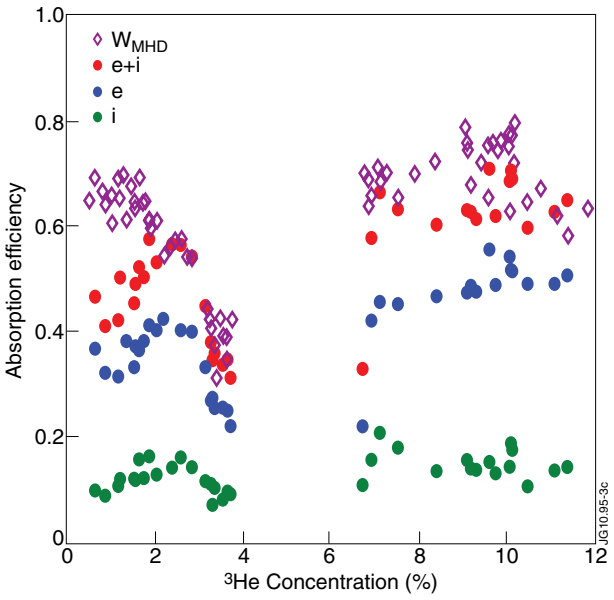

Figure 10: Summary of the absorption efficiencies as a function of the ^{3}He concentration estimate provided by the formula used to steer the real time control gas puffing.

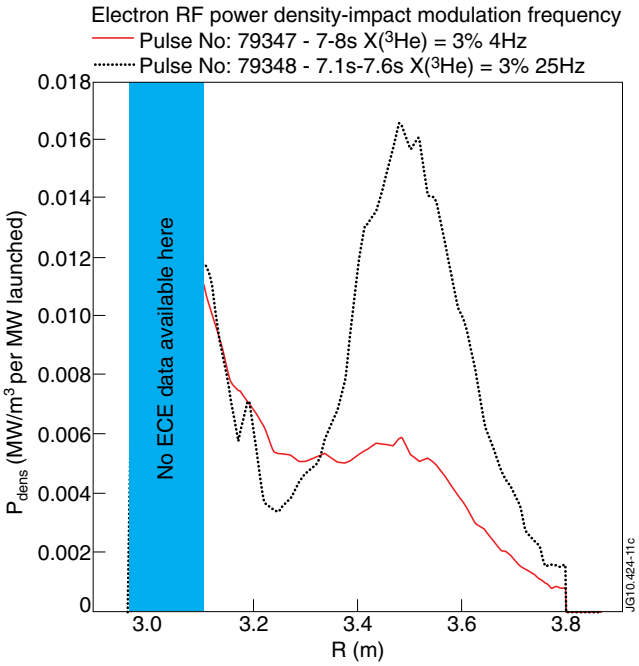

Figure 11: Electron power deposition for a given ^{3}He concentration of 3% but inferred from the electron temperature response to a 4 or 25Hz modulation of the ICRF power launched.

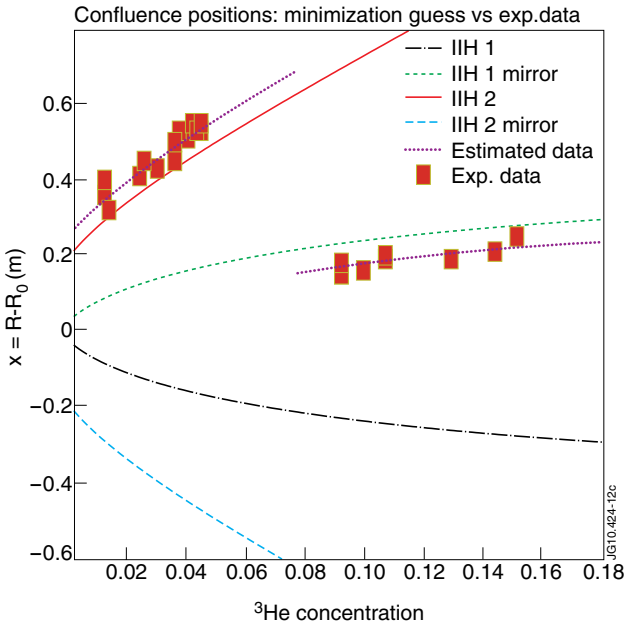

Figure 12: Result of the minimization procedure adjusting the plasma composition to get a dispersion equation fit of the experimental positions (squares) of the confluence region position as a function of the ^{3}He concentration guess provided by the real time control formula.

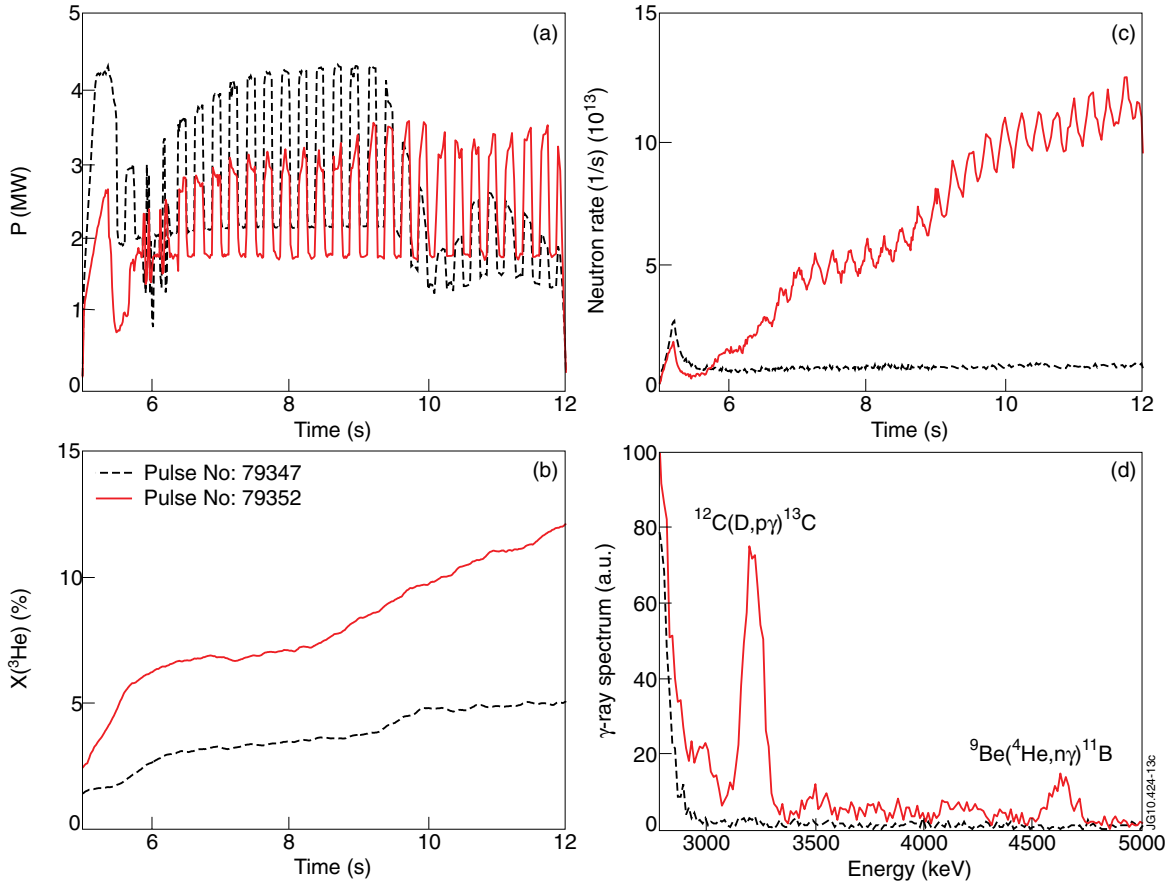

Figure 13: Evidence of ICRF accelerated fast ions, comparison of Pulse No's: 79347 and 79349: (a) ICRF power level, (b) real time control ^{3}He concentration guess, (c) neutron rate, (d) gamma ray spectra (dN/dE as a function of E).

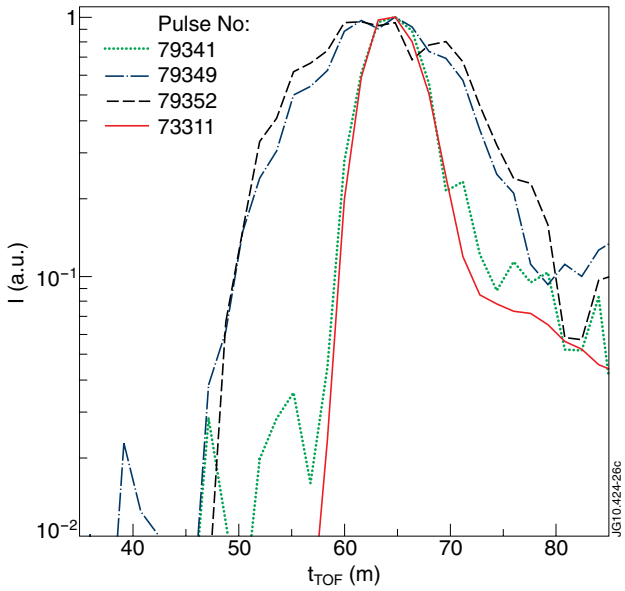

Figure 14: Evidence of ICRF accelerated fast D ions: TOFOR neutron time of flight spectrum for various shots of the (3He)-H minority to mode conversion heating session (low X[^{3}He]: Pulse No: 79341; high X[3He]: Pulse No's: 79349 & 79352), and for a non-ICRF-heated reference shot (Pulse No: 73341).

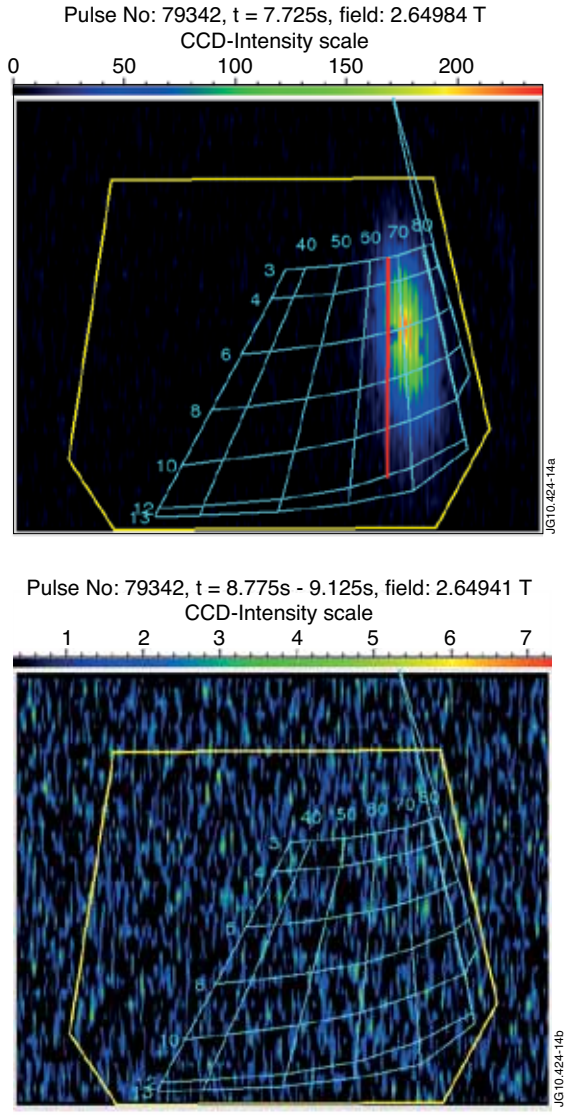

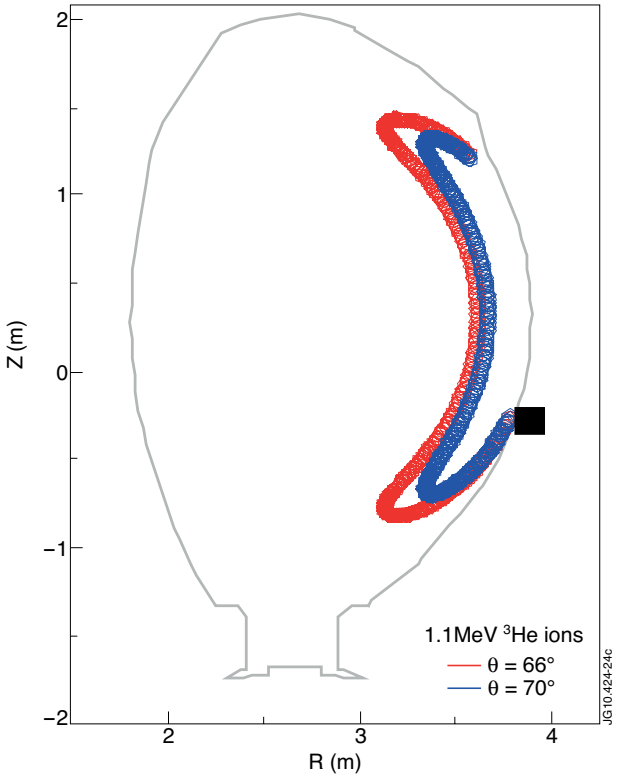

Figure 15: Lost ion detector signal for Pulse No: 79342 (a) at full ICRF power (3.9MW) and (b) during the 25Hz modulation phase resulting in an effective ICRF power of ~2MW. The ^{3}He concentrations are different but similar: 2.0% and 2.5%, respectively. The red line is the location of the ^{3}He non-Doppler-shifted resonance. The trajectories of the ^{3}He particles with energies corresponding to the peak of the number of fast ions detected and hitting the detector plate with two pitch-angles is given in (c).

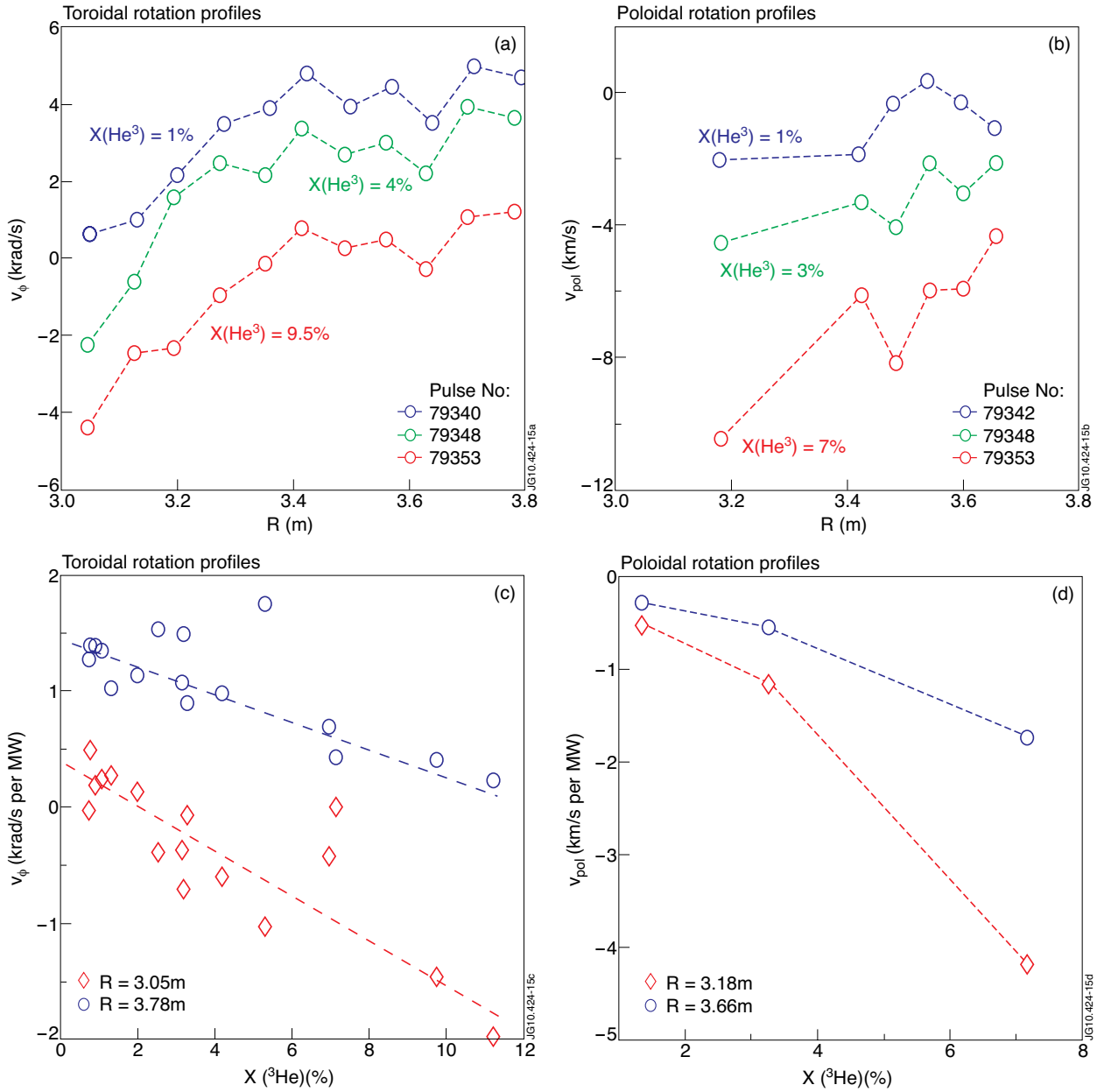

Figure 16: Evidence of ICRF induced toroidal rotation superposed on the plasma's intrinsic rotation: (a&b) toroidal resp. poloidal rotation profiles as a function of the major radius for different ^{3}He concentrations, (c&d) toroidal resp. poloidal rotation profiles as a function of the ^{3}He concentration at different major radii.

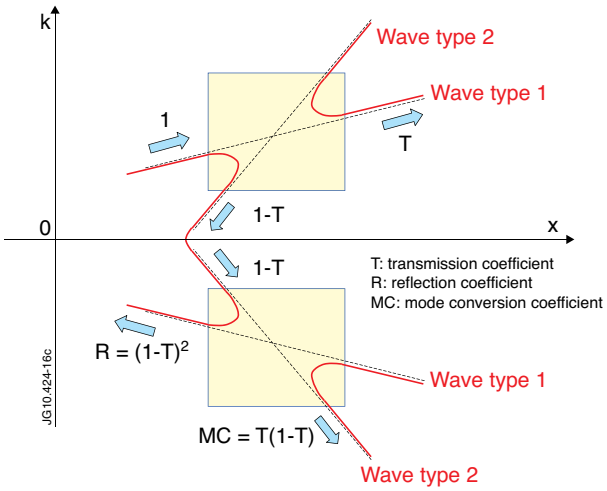

Figure 17: Schematic dispersion root scheme of a 2-wave confluence in the presence of a cutoff of one of the modes.

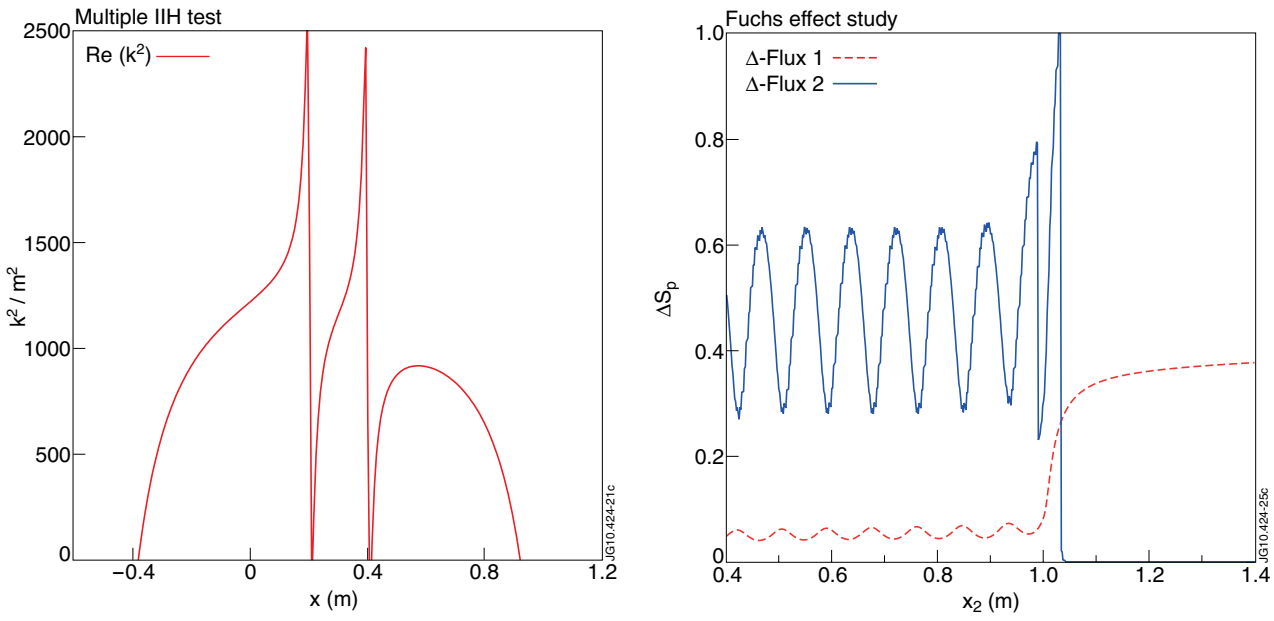

Figure 18: Resonance/confluence coefficients for a double Budden-layer fast wave mock-up: (a) qualitative plot of the square of the dispersion roots, (b) absorption as a function of the location of the x2 confuence/resonance location for xL=-1.0, x1=0 and xR outside the integration interval.

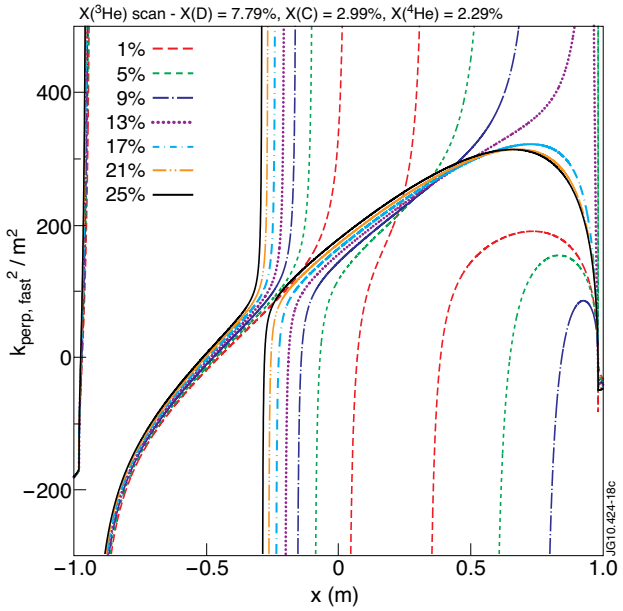

Figure 19: Cold fast wave dispersion equation roots for various ^{3}He concentrations.

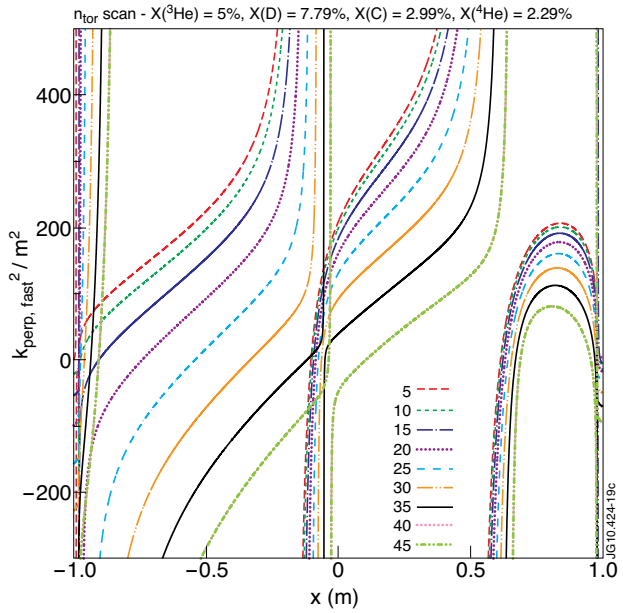

Figure 20: Cold fast wave dispersion equation roots for various toroidal mode numbers.

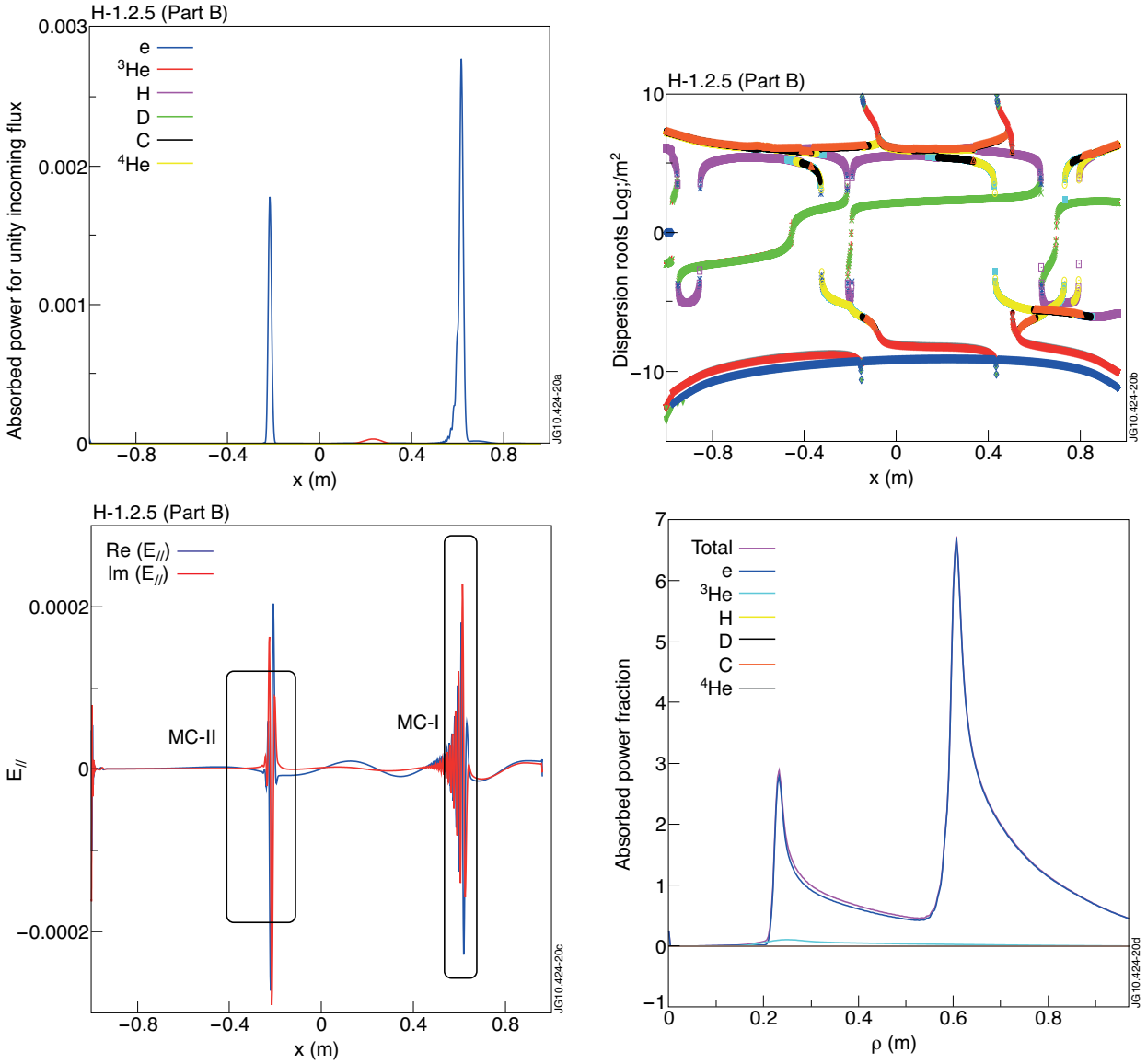

Figure 21: (a) Power deposition profile, (b) dispersion equation roots and (c) parallel electric field for a typical 2-mode conversion layer mode conversion heating scenario. The subfigure (d) shows the deposition profile as a function of the flux surface labeling factor ρ (=half the width of the magnetic surface in the midplane) applying a '2D mock-up' or 'spreading factor' $(1-(Z/a_p)^2)^2$.

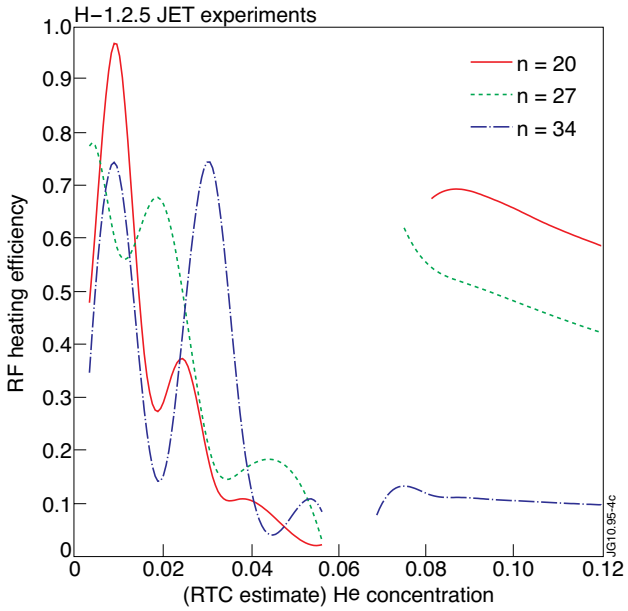

Figure 22: Total ICRF heating efficiency as a function of the ^{3}He concentration using the plasma composition found from the minimization and for 3 toroidal mode numbers inside the main lobe of the dipole phasing antenna spectrum.

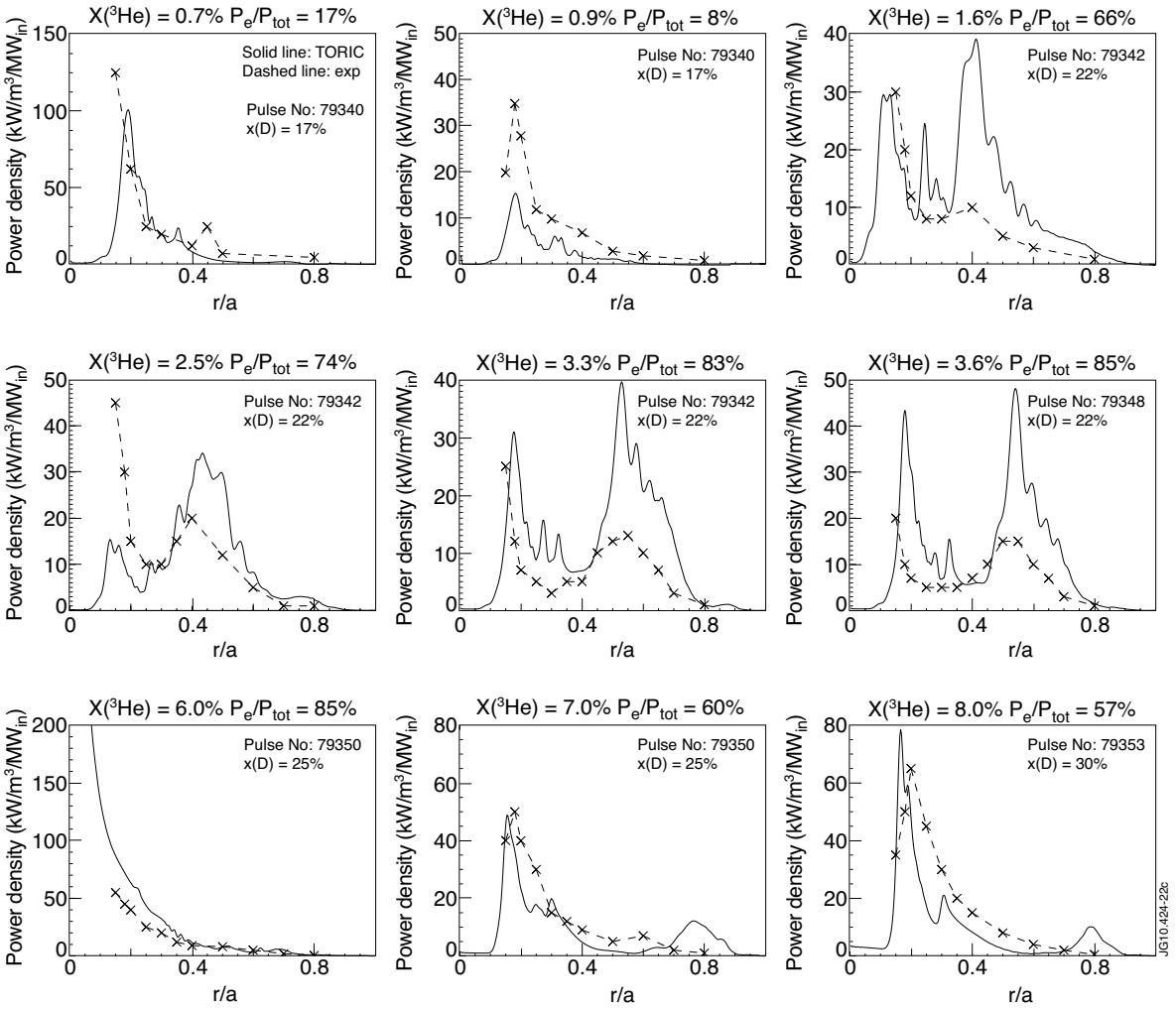

Figure 23: ICRF electron power deposition profile found by TORIC using experimental density and temperature values (solid lines), and experimental electron deposition profiles (dashed line with crosses).